Materials & Design 250 (2025) 113558

Contents lists available at ScienceDirect

Materials & Design

journal homepage: www.elsevier.com/locate/matdes

Mechanical properties and microstructure of wire laser metal deposited austenitic stainless steel

P. Kyvelou [a], W. Hong [a], R. Zhang [a,*], L. Gardner [a]

[a] Department of Civil and Environmental Engineering, Imperial College London, UK

A R T I C L E I N F O

Keywords:
Material anisotropy
Mechanical properties
Metal 3D printing
Microstructural analysis
Stainless steel
Wire laser metal deposition

A B S T R A C T

Laser metal deposition (LMD) is a metal 3D printing method that enables the efficient and cost-effective production of large-scale components, rendering it increasingly attractive for civil engineering applications. However, the scarcity of data and lack of knowledge of the material response and geometric variability of LMD steels is inhibiting adoption of this manufacturing method in the construction industry. To address this, a comprehensive experimental investigation into the geometry, mechanical properties and microstructural characteristics of LMD plates made from ER 308LSi stainless steel has been carried out and is presented herein. Laser scanning, tensile testing and microstructural analyses were conducted on a series of coupons of different thicknesses (2 mm and 8 mm), printing strategies, surface conditions and orientations. The results indicated low geometric irregularity, with both as-built and machined coupons displaying nearly identical mechanical properties. The thinner specimens had lower strengths, mainly attributed to their larger grain sizes. Significant anisotropy was observed from the mechanical tests on the thinner specimens, explained by a strong crystallographic texture observed in the microstructure. Overall, the examined material exhibited good mechanical behaviour and geometric consistency. Finally, a constitutive modelling approach previously applied to wire arc additively manufactured (WAAM) stainless steel was successfully adapted to characterise the anisotropic behaviour of LMD stainless steel in both the elastic and inelastic material ranges. The findings highlight the potential for using LMD in construction, offering a viable means of fabricating large-scale metal components with sound mechanical performance.

1. Introduction

Metal additive manufacturing (AM), popularly known as metal 3D printing, is a rapidly developing technology offering unparalleled production flexibility across a diverse range of sectors. Several methods of metal printing are available. However, in the construction sector, where the production of cost-effective, large-scale components is essential, directed energy deposition (DED) methods are deemed to be the most suitable [1–3]. Among the DED processes, the most prevalent for producing 3D printed metal structural components are wire arc additive manufacturing (WAAM) and wire laser metal deposition (LMD). The high deposition rates inherent to these methods, coupled with the associated low manufacturing costs, enable the fabrication of structural components of practical dimensions at reasonable costs, rendering them ideal for use in the construction sector [4]. Between these two methods, WAAM has higher deposition efficiency, while LMD has been shown to offer superior layer adhesion, ensuring better bonding between layers [5]. This makes LMD more effective in achieving finer details and enhanced mechanical properties in the printed material, though it may be less efficient in terms of material deposition speed compared to WAAM. Despite extensive research into the application of WAAM for structural purposes [6–15], studies focusing on the use of LMD in the construction sector still remain scarce. At the same time, the use of stainless steel in construction is growing owing to its combination of mechanical properties and durability [16–18].

Although wire LMD was originally designed for wear protection [19], it is now emerging as a prominent AM method for fabricating intricate metal components with high precision and structural integrity [20]. Wire LMD operates by directing a high-powered laser beam onto a metal wire, causing it to melt upon contact with the substrate material. This molten metal forms a pool on the substrate, rapidly solidifying to create a solid layer. Wire feeding can be coaxial, where the wire aligns with the laser beam for better precision and flexibility, or non-coaxial, which is simpler and more cost-effective but requires more careful

---

* Corresponding author.
E-mail address: ruizhi.zhang@imperial.ac.uk (R. Zhang).

https://doi.org/10.1016/j.matdes.2024.113558
Received 24 October 2024; Received in revised form 16 December 2024; Accepted 19 December 2024

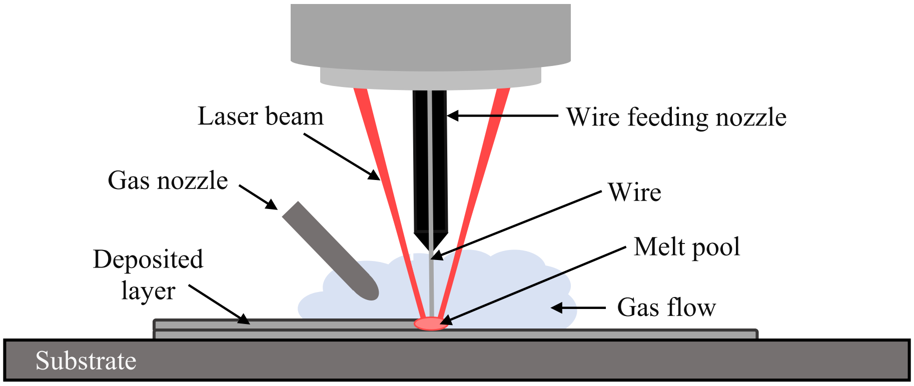

Fig. 1. Schematic illustration of coaxial wire LMD process.

alignment and is less flexible. Coaxial setups are typically preferred for higher precision applications. By carefully controlling the laser beam and wire deposition, complex geometries can be constructed [21,22]. A schematic illustration of the coaxial wire LMD process, as used to produce the specimens studied herein, is shown Fig. 1.

Wire LMD has found numerous applications across industries such as aerospace, automotive and healthcare. In aerospace, it has been used for repairing and refurbishing high-value components like turbine blades and engine casings, thereby extending their operational lifespan and reducing maintenance costs [23]. Similarly, in the automotive sector, wire LMD has been employed for rapid prototyping and low-volume production of specialised components, facilitating accelerated product development cycles and customisation [24]. Furthermore, in healthcare, wire LMD has enabled the fabrication of patient-specific implants and medical devices with intricate geometries, enhancing treatment outcomes and patient comfort [25,26].

Despite its widespread adoption in various industries, the potential of using wire LMD in the construction sector remains largely untapped. Recent advances in AM technologies, coupled with escalating demands for sustainable and cost-effective construction solutions, have spurred interest in utilising LMD for structural engineering applications [27,28]. By fabricating tailored structural components, LMD has the potential to streamline construction processes, minimise material wastage, and enable the realisation of complex architectural designs and optimised structures with high accuracy.

Previous studies [29–32] have revealed strong anisotropy in WAAM stainless steel and have attributed this characteristic primarily to the particular microstructural features resulting from the specific heat profiles experienced during the manufacturing process. Although substantial research has been conducted in recent years to determine the mechanical and structural response of WAAM steels, data on the mechanical properties and microstructure of LMD steels remain rather limited [20,33]. To address this gap and expand the existing experimental database, a comprehensive series of tensile tests and microstructural analyses on LMD stainless steel has been conducted and is presented in this paper. 3D laser scanning and digital image correlation (DIC) were employed to digitally capture the as-built geometric features and deformation responses, respectively, of the LMD tensile coupons, and an in-depth analysis of the geometric, mechanical and microstructural characteristics of the examined LMD material is described.

2. Manufacturing and preparation of test specimens

2.1. Manufacturing process

Printing of the specimens was undertaken by the Spanish company Meltio, using their proprietary multi-axis robotic coaxial LMD technology [34]. Flat plates of two different nominal thicknesses t_{nom} – 2 mm and 8 mm – were manufactured using ER 308LSi (EN ISO 14343-A – G 19 9 LSi) austenitic stainless steel feedstock wire of 1 mm diameter. The chemical composition of the feedstock material, as provided by the manufacturer, is reported in Table 1, while the process parameters adopted during additive manufacturing are presented in Table 2. A 400 × 300 × 20 mm AISI304 stainless steel plate was adopted as the substrate. Regarding the adopted printing strategy, the thin plates (i.e. $t_{nom} = 2$ mm) were printed with single passes, while for the thick plates (i.e. $t_{nom} = 8$ mm) the perimeter was first deposited, followed by the infill interspersed with angles of 45° and −45°. Note that the plates of 2 mm thickness were extracted from oval tubes with flat sides – see Fig. 2, while the plates of 8 mm thickness were additively manufactured as a single wall.

Table 1
Chemical composition (in % by weight) of feedstock wire, as provided by the manufacturer.

Feedstock wire	C	Si	Mn	Cr	Ni	Fe
ER 308LSi	0.02	0.90	1.70	20	10	Balance

Table 2
Process parameters used for LMD plates.

Process parameters	$t_{nom} = 2$ mm	$t_{nom} = 8$ mm
Travel speed (mm/s)	10	7.5
Wire feed speed (mm/s)	15.1–15.3	7.6–9.6
Laser power (W)	800–830	1100
Time between layers (s)	25	25
Layer height (mm)	0.6	1.0
Layer width (mm)	2.0	1.0

2.2. Specimen preparation

Tensile coupons, dimensioned in line with EN ISO 6892–1 [35], were extracted from the LMD plates using a water jet cutter, as depicted in Fig. 3(a), and then sandblasted, as shown in Fig. 3(b). To evaluate the influence of the surface undulations, which are a characteristic of the DED wire processes, on the material properties of the LMD specimens, certain plate sections were machined to achieve a smooth surface finish – see Fig. 3(c) and 3(d), while others were tested in the as-built condition. Finally, in order to examine the degree of material anisotropy, tensile coupons were extracted from the parent plates at three different orientations (i.e. 0°, 45° and 90°) relative to the print layer orientation, as illustrated in Fig. 4.

The coupon designation system begins with the letters ‘AB’ or ‘M’ to denote the as-built (i.e. undulating) or machined (i.e. smooth) surface condition of the coupon, followed by the nominal thickness in mm, the angle of coupon extraction relative to the print layer orientation in degrees, as defined in Fig. 4, and, finally, a number to identify each

(a) (b)

Fig. 2. Oval tubes of 2 mm thickness with flat sides: (a) front view and (b) top view.

(a) (b) (c) (d)

Fig. 3. Preparation of tensile coupons: (a) waterjet cutting, (b) sandblasting, (c) as-built (top) and machined (bottom) plate before sandblasting, (d) as-built and machined plate after sandblasting.

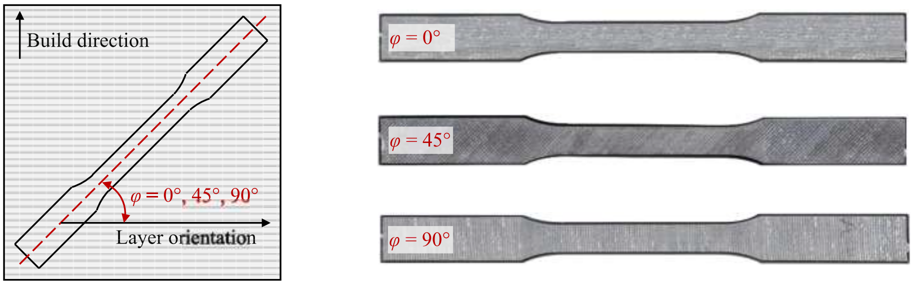

(a) (b)

Fig. 4. Orientations of extracted tensile coupons: (a) angle definition, (b) typical coupons of different orientations.

individual coupon originating from the plate. For instance, coupon AB-2–0-2 is the second as-built coupon with a nominal thickness of 2 mm, extracted at a 0° angle to the print layer orientation. In total, 33 tensile coupons of different surface finishes, thicknesses and orientations were tested, as summarised in Table 3.

3. Physical properties

The density of the LMD stainless steel was assessed based on Archimedes' principle, providing an indication of the average porosity of the printed material. To accurately determine the geometric properties of the tensile specimens, 3D laser scanning was employed, since the undulating as-built LMD surfaces rendered conventional measurement instrumentation inaccurate. The accuracy of the laser scan data was verified by comparing the specimen volumes derived from the laser scans with those obtained using Archimedes' principle. Subsequently, geometric analysis was performed on the laser-scanned data to ascertain the mean dimensional properties and quantify the geometric variability of the LMD specimens. The setups employed for the measurement of the physical properties of the examined specimens are described in this section and illustrated in Fig. 5.

3.1. *Density measurements*

The density of the LMD specimens was determined based on Archimedes' principle, following the methodology outlined in [8,36,37]. The

Table 3
Examined parameters of the tested LMD stainless steel coupons.

Nominal thickness (mm)	Surface finish	Coupon orientation φ (°)	Coupon ID	No. of coupons
2.0	As-built	0	AB-2-0	3
		45	AB-2-45	3
		90	AB-2-90	3
	Machined	0	M-2-0	3
		45	M-2-45	3
		90	M-2-90	3
8.0	As-built	0	AB-8-0	2
		45	AB-8-45	3
		90	AB-8-90	3
	Machined	0	M-8-0	2
		45	M-8-45	2
		90	M-8-90	3

density was determined using the setup shown in Fig. 5(a), as the mass of the measured specimen divided by its volume, which was derived based on the mass of the water displaced when the specimen was submerged in a water bath. Three representative test specimens per nominal thickness were used to provide repeated density measurements. The average densities ρ for the 2 mm and 8 mm thick specimens were equal to 7860 kg/m^3 and 7870 kg/m^3 respectively, which were consistent and only slightly lower than the standard density value of $\rho_0 = 7900$ kg/m^3 for conventional stainless steels, indicating a very low average level of porosity.

3.2. Geometric analysis

A Faro ScanARM equipped with a FARO laser line probe was utilised to obtain laser scans of all tensile specimens. This setup offers rapid data capture of up to 500,000 points per second, with an accuracy of 0.1 mm and a resolution of 0.075 mm. The laser scanning process for a typical specimen is illustrated in Fig. 5(b). The scan data of each specimen, represented as a point cloud, were converted into a polygon object using the software Geomagic Wrap [38] and then imported into Rhino 3D [39] for geometric analysis; this was caried out following the process described in [36,37]. Following alignment of the longitudinal axis of each tensile coupon with the global x axis, cross-section contours along the parallel length were taken at 0.1 mm intervals [36,37]. At each cut i, the cross-sectional area A_i and eccentricities $e_{y,i}$ and $e_{z,i}$ of the cross-sectional centroid along the global y and z axes respectively, relative to the overall centroidal axis of the coupon, were calculated – see Fig. 6. The thickness values t_{ij} within each cross-section were determined as the distances between all opposing cross-sectional points j, as shown in Fig. 6. The average thickness of each cross-section t_i was determined as the mean of the t_{ij} values at each cut i.

The average geometric properties of the as-built coupons are summarised in Table 4, grouped by nominal thickness t_{nom} and coupon extraction orientation φ, as defined in Fig. 4. In Table 4, A, A_{min} and A_{sd}, and t, t_{min} and t_{sd}, are the average, minimum and standard deviation values of the cross-sectional area and thickness respectively, $|e_y|$ is the average centroid eccentricity magnitude along the y axis (as per Fig. 6), and $|e_z|$, $|e_z|_{max}$ and $|e_z|_{sd}$ are the average, maximum and standard

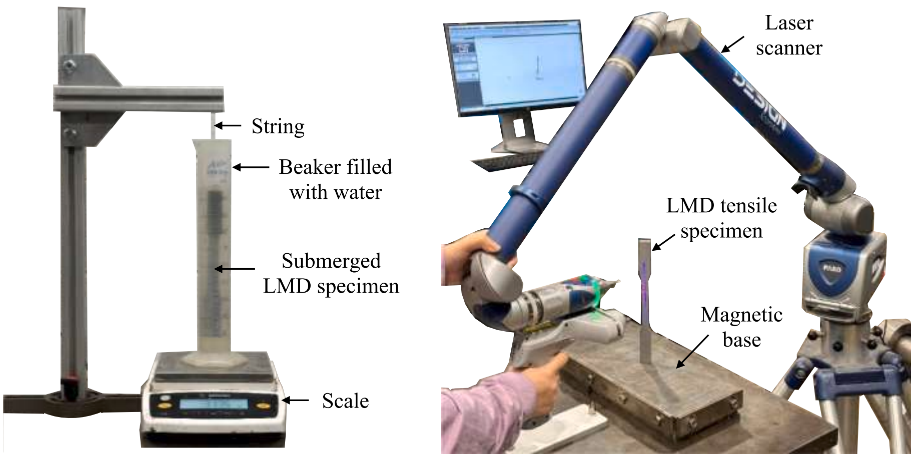

(a) (b)

Fig. 5. Employed setup for the determination of physical properties: (a) density measurements and (b) 3D laser scanning.

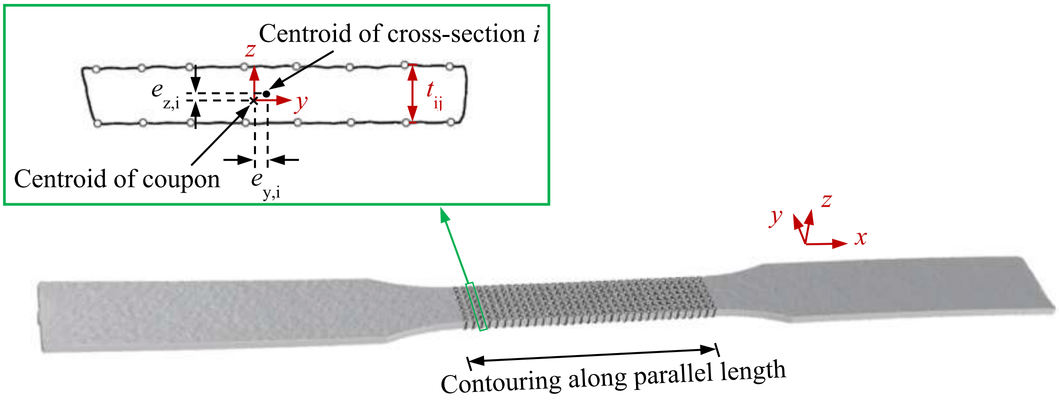

Fig. 6. Typical processing of coupon geometry in Rhino 3D.

Table 4
Average geometric properties of as-built coupons.

t_{nom} (mm)	φ (°)	A (mm^2)	$\frac{A_{min}}{A}$	$\frac{A_{sd}}{A}$	t (mm)	$\frac{t_{min}}{t}$	$\frac{t_{sd}}{t}$	$\frac{\lvert e_y \rvert}{t}$	$\frac{\lvert e_z \rvert}{t}$	$\frac{\lvert e_z \rvert_{max}}{t}$	$\frac{\lvert e_z \rvert_{sd}}{t}$
2	0	23.9	0.97	0.010	1.92	0.92	0.025	0.034	0.073	0.094	0.014
	45	24.5	0.99	0.006	1.93	0.95	0.014	0.016	0.251	0.378	0.090
	90	24.7	0.98	0.006	1.95	0.94	0.014	0.092	0.484	0.622	0.114
8	0	98.4	0.99	0.005	7.83	0.97	0.012	0.006	0.003	0.008	0.002
	45	98.5	0.99	0.003	7.74	0.96	0.011	0.007	0.006	0.012	0.002
	90	98.1	0.99	0.006	7.81	0.97	0.008	0.008	0.007	0.016	0.003

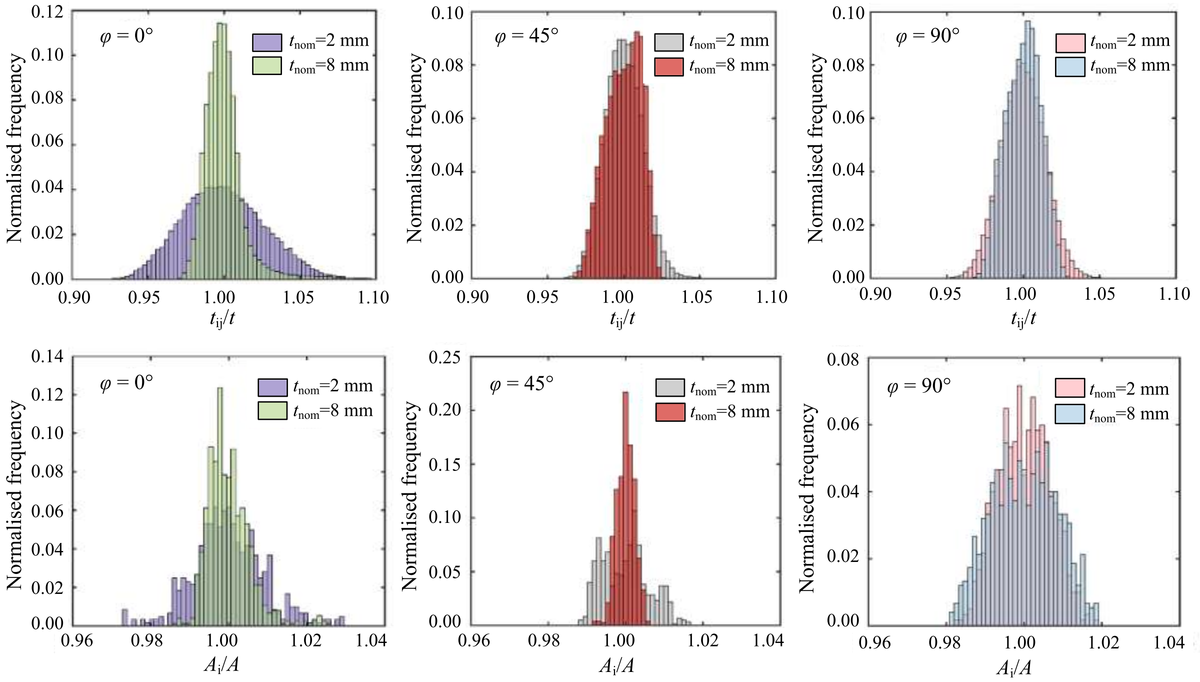

Fig. 7. Distribution of normalised thicknesses and cross-sectional areas of typical as-built coupons.

deviation values of the eccentricity magnitude along the z axis respectively. It can be observed that the variation in the cross-sectional areas and thicknesses across all tensile coupons is low and relatively uniform, suggesting minimal geometric irregularity in the LMD specimens. The A_{min}/A values range from 0.97 to 0.99, highlighting the excellent geometric consistency. This uniformity is attributed to the concentrated and relatively low heat input in the LMD process, which ensures that the geometric properties remain consistent throughout the specimen. As expected, the eccentricities measured in the y direction $|e_y|$ were generally significantly lower than those in the z direction $|e_z|$. Finally, as can be seen from the values reported in Table 4, the maximum centroid eccentricities, as well as their standard deviations, were found to slightly increase with increasing values of φ. It should be mentioned that similar studies on WAAM austenitic stainless steel of the same grade have reported greater geometric variability [36,15], which is attributed to the higher heat input and less controlled deposition of the WAAM process.

Fig. 7 presents histograms of the measured thicknesses and cross-sectional areas of typical coupons, with the individual cross-sectional thickness measurements t_{ij} and the area measurements A_i normalised by the corresponding average coupon thickness t and cross-sectional area A respectively. The histograms reveal a lower spread of thickness for the thicker coupons (i.e. $t_{nom} = 8$ mm) compared to the thinner coupons (i.e. $t_{nom} = 2$ mm), which can be also confirmed by the lower values of t_{sd}/t of the thicker coupons – see Table 4. This discrepancy is attributed to the different printing strategies used for the different wall thicknesses, with the single-pass method employed for the thinner specimens resulting in more pronounced surface undulations. Similar findings were reported by Weber *et al.* [8] for single-pass printing using WAAM.

It can also be observed that, apart from the $\varphi = 0°$ coupons, which exhibit a slightly wider thickness distribution, the other coupons show similarly scattered thickness distributions, as indicated by the comparable t_{sd}/t values reported in Table 4. As expected, the variation in cross-sectional area is less pronounced than that in thickness, as illustrated by the histograms in Fig. 7 and confirmed by the A_{sd}/A values in Table 4.

4. Microstructural analysis and microhardness testing

The rapid solidification of LMD metals, which is a typical feature across all DED processes, can significantly influence the microstructure and, consequently, the material properties of additively manufactured steels [36,40]. Therefore, to better understand the mechanical behaviour of the LMD material examined herein, its microstructural characteristics were examined.

4.1. Employed techniques and methods

Metallographic samples in the SD-BD, TD-BD and SD-TD planes were extracted from the middle of the 2 mm and 8 mm LMD plates and mounted in bakelite, with the SD and BD axes being parallel to the deposition layer (i.e. the scanning direction) and build direction respectively, and the TD axis being perpendicular to the plate thickness –

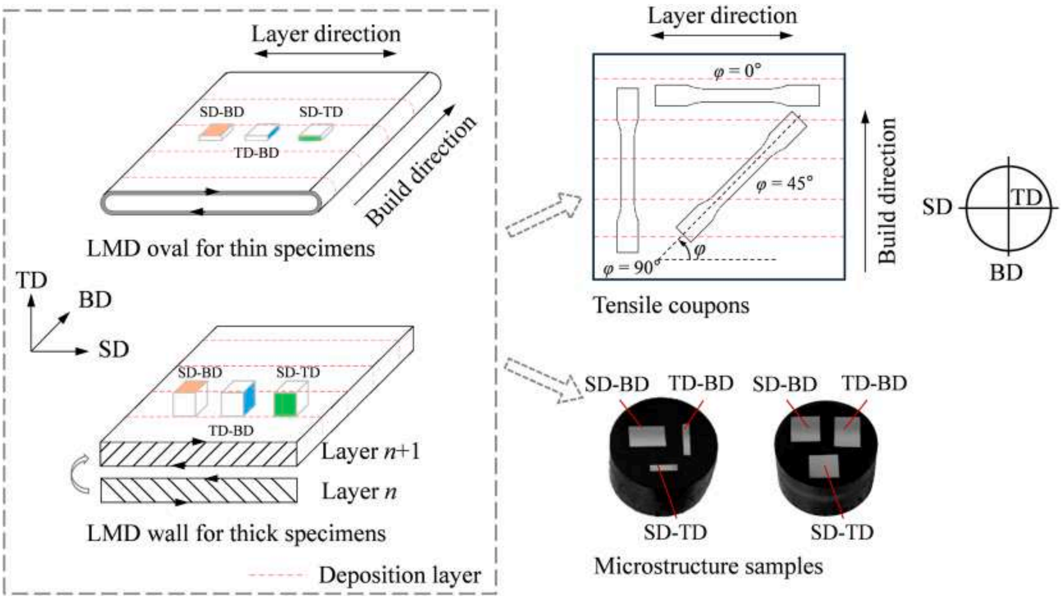

Fig. 8. Schematic illustration of LMD specimens and extraction of coupons and metallographic samples.

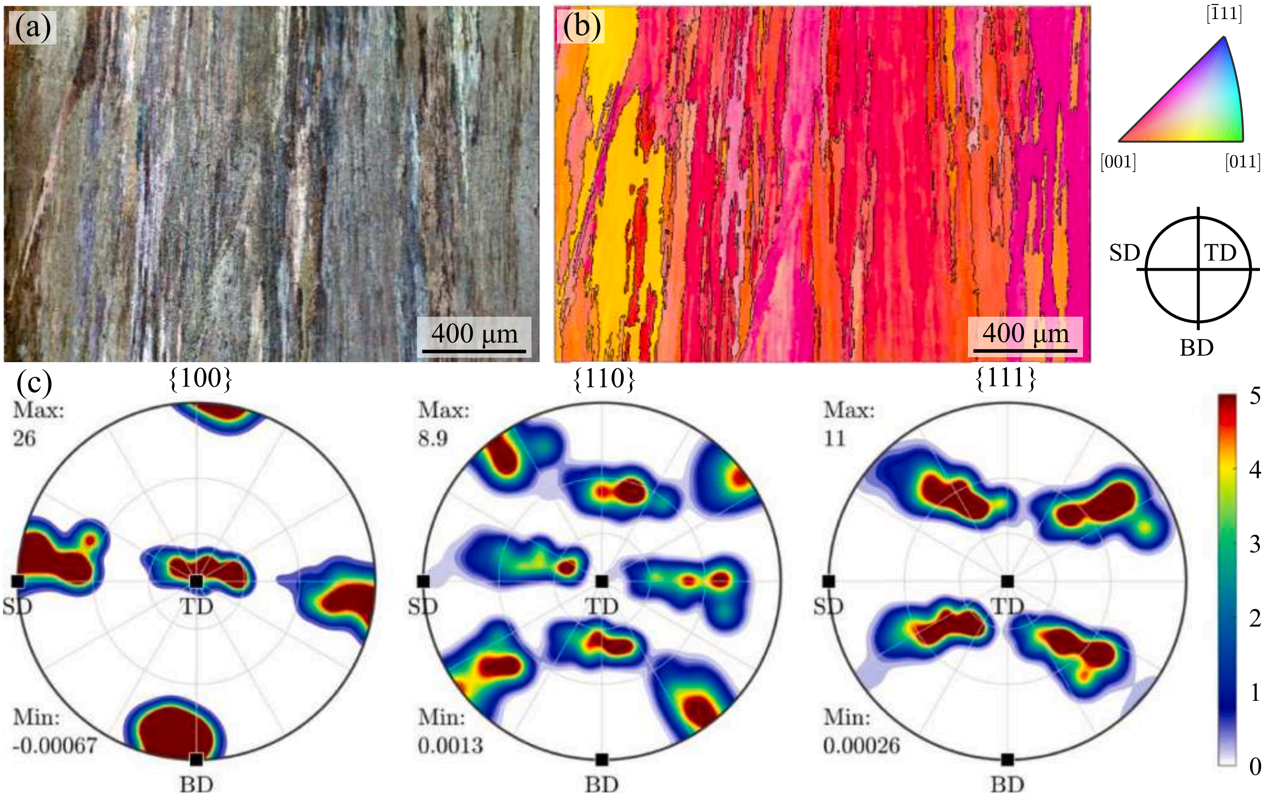

Fig. 9. 2 mm LMD stainless steel sample: (a) FSD map, (b) crystal orientation map in the SD-BD plane presented as IPF map relative to the build direction (IPF-BD) with boundaries overlaid, and (c) {100}, {110} and {111} pole figures.

see Fig. 8. The samples were prepared for microstructural analysis using the standard metallographic procedures specified in ASTM E3-11 [41], including mechanical grinding with silicon carbide papers from 500 to 4000 grit size and polishing with 3 μm and 1 μm diamond suspensions and finally a mixture of 0.04 μm OP-S colloidal silica solution (H_2O_2: OPS:H_2O = 3:7:10) until a flat and scratch-free surface was achieved. The crystal orientations and texture were obtained using an FEI Quanta FEG 650 scanning electron microscope (SEM) equipped with a Bruker eFlash^{HD} EBSD detector and Argus forescatter diodes (FSD) imaging. The polished samples were tilted to 70° relative to the horizontal plane and observed using the SEM, operating at 20 kV acceleration voltage, with a 15 mm working distance and a 100 μm aperture size. FSD images were then taken using a detector tilt of 10.3° and a detector distance of 19.7 mm, highlighting the contrast for the surface topography and crystal orientation. The SD-BD plane of the samples was scanned for EBSD at 100 × magnification over an area of 2059 × 1372 μm^2 with a 2.57 μm

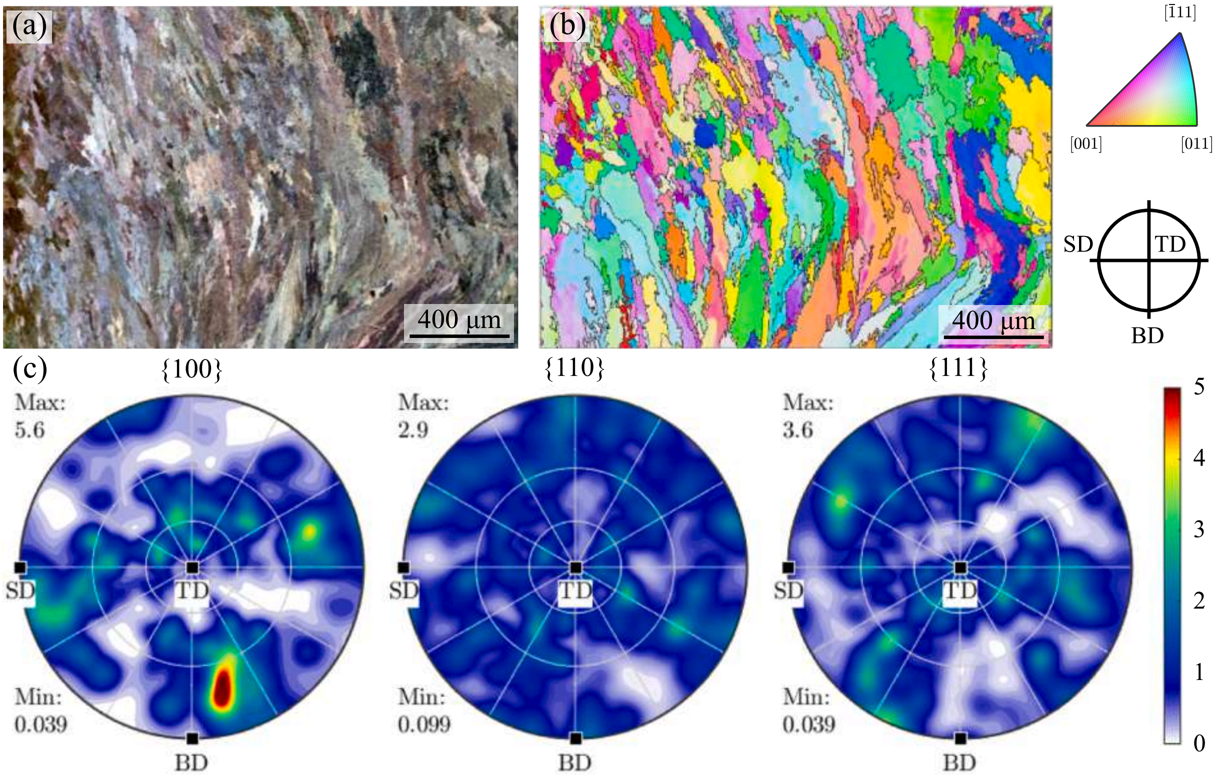

Fig. 10. 8 mm LMD stainless steel sample: (a) FSD map, (b) crystal orientation map in the SD-BD plane presented as IPF map relative to the build direction (IPF-BD) with boundaries overlaid, and (c) {100}, {110} and {111} pole figures.

step size, to avoid losing substructure details while ensuring sufficient grain coverage. The EBSD patterns were acquired with a minimum 90% indexing using the acquisition software Esprit 2.2 [42], and grains were reconstructed considering a 5° misorientation threshold to replace the unindexed measurement points in the Matlab toolbox MTEX [43].

4.2. Microstructural characterisation

The EBSD results for the 2 mm and 8 mm LMD stainless steel in the SD-BD plane are shown in Figs. 9 and 10 respectively, including the local crystal orientations represented as inverse pole figure (IPF) maps coloured with respect to the build direction (IPF-BD), with overlaid grain boundaries and the global crystallographic texture expressed by {100}, {110} and {111} pole figures.

The SD-BD plane of the 2 mm stainless steel exhibited a microstructure dominated by long columnar grains crossing several build layers, which are shown in red in the IPF map in Fig. 9(b). These grains showed a preferred orientation of [001] aligned with the build direction, which can be attributed to the plate being produced layer by layer along the BD axis, as grains typically follow the highest thermal gradient during the solidification process. This preferred orientation was further confirmed by the {100} pole figure of the 2 mm LMD stainless steel in the SD-BD plane, shown in Fig. 9(c), where high concentrations of the {100} plane normals (i.e. [001], [00$\bar{1}$], [100], [$\bar{1}$00], [010] and [0$\bar{1}$0]) directions) along the SD (i.e. $\varphi = 0^\circ$), TD and BD (i.e. $\varphi = 90^\circ$) axes were found, indicating a strong <100> crystallographic texture. From the {110} pole figure, a large proportion of grains with a <110> texture was found to closely align with the $\varphi = 45^\circ$ direction. Note that similar metallurgical characteristics have been reported in previous studies on WAAM 308LSi stainless steel [35].

The FSD map, IPF map coloured with respect to the build direction and the {100}, {110} and {111} pole figures for the 8 mm LMD stainless steel in the SD-BD plane are shown in Fig. 10. The microstructure was found to feature columnar grains of different aspect ratios, with their long axes oriented either roughly parallel to BD or at 45° relative to BD; this can be attributed to the employed printing strategies and local heat flow. As can be seen from the pole figures, the 8 mm LMD stainless steel demonstrated a weak texture with no clear preferred crystallographic orientation. Compared with the strong texture found in 2 mm stainless steel, this indicates that the different printing strategy employed had a significant influence on the crystallographic texture.

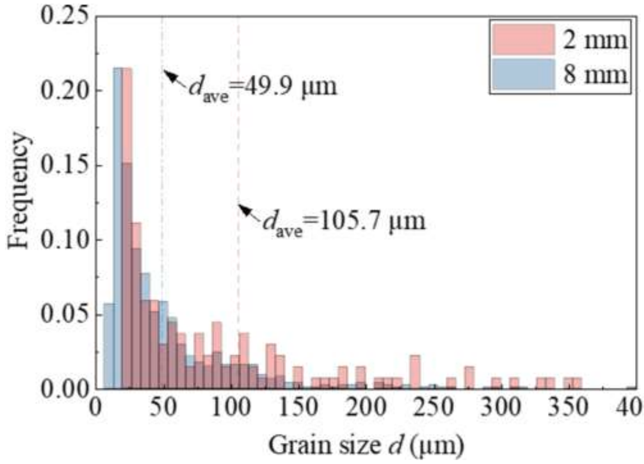

Fig. 11. Grain size distribution of LMD stainless steel samples of 2 mm and 8 mm thicknesses.

The grain size *d*, defined as the diameter of an equivalent circle of the same area as the grain, was determined using EBSD in accordance with ASTM: E2627-23 [44]. The grain size distributions in the scanned areas of the 2 mm and 8 mm LMD stainless steel samples in the SD-BD plane are shown in Fig. 11. The average grain sizes, which were found to be influential on the mechanical properties (see Sections 6 and 7), were

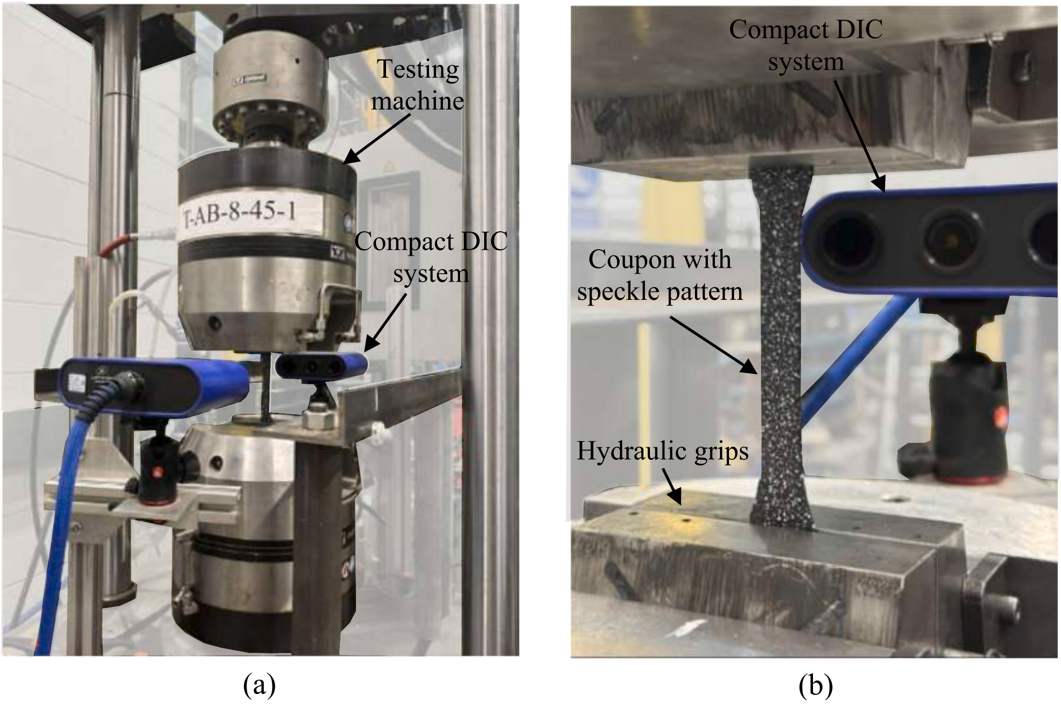

Fig. 12. Experimental setup for tensile testing: (a) overall view and (b) close up view.

measured to be 105.7 µm and 49.9 µm respectively.

4.3. Microhardness testing

To investigate the effect of the printing strategy on the hardness of the printed material, microhardness tests were performed on polished samples in accordance with EN ISO 6507–1 [45], using a Wilson VH1202 hardness tester equipped with an optical microscope. Three Vickers hardness measurements per nominal thickness were taken, with each indentation made at a load of 4.9 N (i.e. 500 gf) applied for 10 s. The mean measured microhardness values for the 2 mm and 8 mm samples were 178 $HV_{0.5}$ and 185 $HV_{0.5}$ respectively, with the individual measurements being 176 $HV_{0.5}$, 182 $HV_{0.5}$ and 177 $HV_{0.5}$ for the 2 mm samples and 188 $HV_{0.5}$, 190 $HV_{0.5}$ and 175 $HV_{0.5}$ for the 8 mm samples. The different printing strategies adopted for the 2 mm and 8 mm LMD stainless steels were found to have no significant influence on the microhardness, although the 8 mm LMD stainless steel exhibited a slightly higher value of microhardness.

5. Tensile coupon tests

The monotonic stress–strain properties of the LMD stainless steel specimens were determined at room temperature in line with EN ISO 6892–1 [35] in the Structures Laboratory of the Department of Civil and Environmental Engineering at Imperial College London. The employed experimental setup is described in this section, followed by a detailed analysis of the obtained results.

5.1. Test setup

All tensile tests were carried out using an Instron 8802 250 kN hydraulic testing machine with hydraulic grips, operating in displacement control. The adopted displacement rate was determined in line with EN ISO 6892–1 [35], with a strain rate of 0.00007 s^{-1} up to the 0.2% proof strength $\sigma_{0.2}$ of the material [46,47], gradually increased with three intermediate steps to 0.00025 s^{-1} until fracture. Overlapping standard gauge lengths equal to $5.65\sqrt{A}$ [35], where A was taken as the average cross-sectional area of the parallel length as obtained by laser scanning (see Section 3.2), were marked onto the two sides of each coupon for the calculation of the fracture strain ε_f after testing.

The strain and displacement fields along the parallel length on both sides of the coupon specimens were monitored using a four-camera StrainMaster Compact digital image correlation (DIC) system from LaVision, equipped with two cameras and an integrated LED illumination source on each side. The DIC setup is illustrated in Fig. 12. Both faces of the coupons were prepared for DIC image acquisition by first spraying them with black matt paint along the parallel length to minimise reflection during image capture and then applying a random pattern of white speckles for their relative movement between sequential images to be tracked. The tensile load, measured by a load cell within the Instron testing machine, was transmitted to the DIC system through an analogue to digital converter. During testing, the load readings and DIC images were synchronously recorded at a frequency of 1 Hz using the DaVis 10 software package [48].

After testing, the acquired images and load data were processed using DaVis by tracking the relative movements of the surface speckles between sequential frames to determine the strain distribution for each frame. This process enabled the generation of an average stress–strain curve for each specimen, with the average stress calculated as the applied load divided by the average original cross-sectional area A, and the average strain measured over the full parallel length of both sides of each coupon. Note that the use of DIC for the conducted tests was particularly important for investigating whether the strain field in LMD stainless steel under macroscopic uniaxial loading is uniform as for conventionally produced steels, or more similar to the non-uniform strain fields observed in WAAM steels [8,36].

5.2. Test results

The mechanical properties and engineering stress–strain curves of the tested LMD coupons are presented and discussed in this section. Key mechanical parameters were determined based on the obtained test data, following the process described by Kyvelou *et al.* [36]. Note that to reduce the experimental noise in the raw data obtained from the DIC

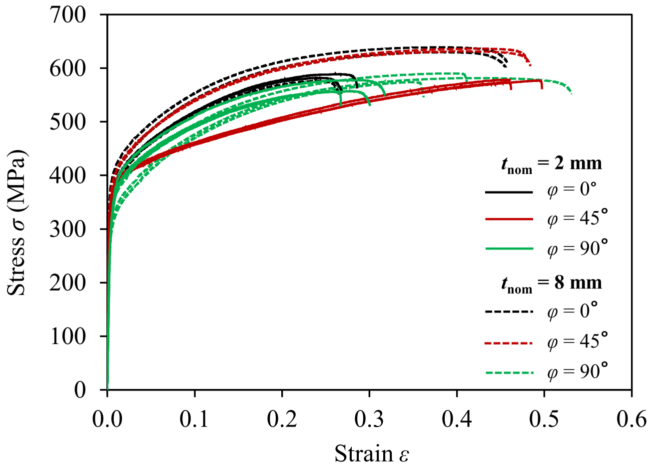

(a) Full range

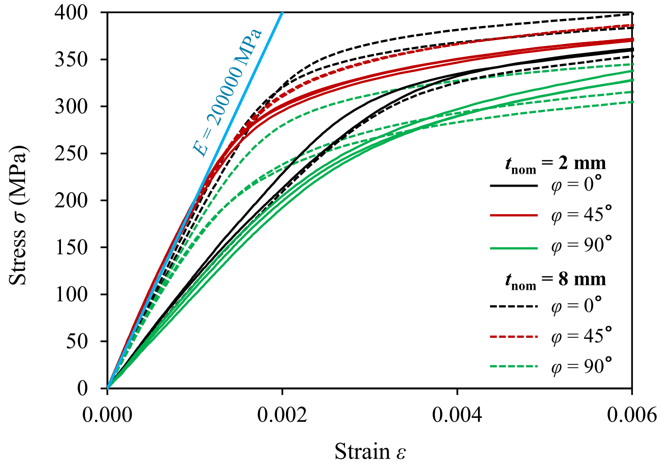

(b) Initial range

Fig. 13. Stress–strain curves from machined coupons.

system, a moving average filter of 15 data points was applied. Given the roundedness of the stainless steel stress–strain curves [49], the two-stage Ramberg-Osgood material model was employed for the description of the material response of the tested coupons [46,47,49–51]. The Young's modulus was determined by regression analysis as described in [36], the yield stress was taken as the 0.2% proof stress, while the Poisson's ratio ν was defined based on the ratio of the mean transverse to mean longitudinal strains within the elastic range (between about $0.1\sigma_{0.2}$ and $0.3\sigma_{0.2}$). The stress–strain characteristics of the LMD material were found to be influenced by the employed printing strategy, wall thickness and direction of coupon extraction.

5.2.1. *Machined coupons*

The full stress–strain curves of the machined coupons are presented in Fig. 13(a), while the elastic range and initial yielding are shown in Fig. 13(b), where the typical value of $E = 200000$ MPa for conventional stainless steels [52] is also plotted. The mechanical properties of all machined coupons are listed in Table 5, where E is the Young's modulus, $\sigma_{0.2}$ is the 0.2% proof stress, σ_u is the ultimate tensile strength, ε_u is the strain at σ_u, n and m are the strain hardening exponents of the two-stage Ramberg-Osgood material model, ε_f is the fracture strain and ν is the Poisson's ratio. A summary of the average material properties grouped by nominal thickness t_{nom} and direction of loading relative to the print layer orientation φ are reported in Table 6.

Overall, the tested coupons demonstrated good ductility, meeting the Eurocode 3 ductility requirements for stainless steels, namely $\sigma_u/\sigma_{0.2} \geq 1.10$, $\varepsilon_f \geq 15\%$ and $\varepsilon_u/\varepsilon_y \geq 15$ (where $\varepsilon_{y=}\ \sigma_{0.2}/E$ is the yield strain), as set out in EN 1993–1-4 [52,53]. The results from the three tested orientations reveal clear material anisotropy, as apparent from Fig. 14 and Table 6. The coupons tested in the 45° orientation generally exhibited superior mechanical properties compared to the coupons tested in the 0° and 90° directions. The largest differences were observed for the Young's modulus, with the E values of the 45° coupons being approximately 45% and 10% higher than those of the other tested orientations for the thinner and thicker coupons, respectively. Similar trends were observed for the elongation at fracture ε_f. For the yield and ultimate strengths, the differences were smaller, with the most pronounced differences observed for the yield strength of the 90° coupons (approximately 10% and 20% lower than the 45° coupons for the thinner and thicker material respectively). The Poisson's ratios were measured to be close to zero in the 45° coupons, indicating the development of negligible transverse strains when loaded longitudinally within the elastic range; this behaviour is attributed to the preferred crystallographic orientations in the 45° directions, specifically the prevalence of crystals aligned along the <110> directions.

5.2.2. *As-built coupons*

The full engineering stress–strain curves of the as-built coupons are plotted in Fig. 14(a), while their initial portions are shown in Fig. 14(b). The mechanical properties of all as-built coupons are listed in Table 7, while a summary of the average material properties grouped by nominal thickness t_{nom} and direction of loading relative to the print layer orientation φ are reported in Table 8. For both tables, the employed notation follows the same convention as in Tables 4 and 5. Note that, due to the geometric undulations of the as-built surface, the material

Table 5
Mechanical properties of machined coupons.

Coupon ID	E (MPa)	$\sigma_{0.2}$ (MPa)	σ_u (MPa)	ε_u	ε_f	n	m	ν	$\sigma_u/\sigma_{0.2}$	$\varepsilon_u/\varepsilon_y$
M-2-0-1	122,100	348	589	0.27	0.38	9.1	2.9	0.402	1.69	94.7
M-2-0-2	114,600	342	576	0.24	0.33	7.0	2.7	0.395	1.68	80.4
M-2-0-3	121,700	349	582	0.24	0.35	5.4	2.6	0.451	1.67	83.7
M-2-45-1	217,400	345	578	0.46	0.53	7.7	2.4	−0.028	1.68	289.9
M-2-45-2	201,400	341	577	0.49	0.50	8.6	2.5	−0.054	1.69	289.4
M-2-45-3	217,000	344	574	0.46	0.52	7.6	2.3	−0.042	1.67	290.2
M-2-90-1	107,300	309	556	0.26	0.27	6.4	3.4	0.348	1.80	90.3
M-2-90-2	113,100	316	578	0.29	0.31	5.7	3.7	0.394	1.83	103.8
M-2-90-3	99,600	315	557	0.28	0.31	7.0	3.3	0.349	1.77	88.5
M-8-0-1	188,100	368	630	0.38	0.50	13.5	3.3	0.326	1.71	194.2
M-8-0-2	178,500	382	639	0.38	0.50	14.0	3.3	0.304	1.67	177.6
M-8-45-1	202,400	363	631	0.42	0.52	9.3	3.4	0.268	1.74	234.2
M-8-45-2	201,800	362	636	0.43	0.50	8.9	3.3	0.266	1.76	239.7
M-8-90-1	175,500	325	590	0.40	0.43	9.8	3.2	0.311	1.82	216.0
M-8-90-2	170,000	287	582	0.42	0.57	6.1	3.3	0.373	2.03	248.8
M-8-90-3	174,900	277	574	0.35	0.38	6.1	3.0	0.361	2.07	221.0

Table 6
Average mechanical properties of machined coupons.

t_{nom} (mm)	φ (°)	E (MPa)	$\sigma_{0.2}$ (MPa)	σ_u (MPa)	ε_u	ε_f	n	m	ν	$\sigma_u/\sigma_{0.2}$	$\varepsilon_u/\varepsilon_y$
2	0	119,400	346	582	0.25	0.35	7.2	2.7	0.416	1.68	86.3
	45	211,900	343	577	0.47	0.52	8.0	2.4	−0.041	1.68	289.8
	90	106,700	313	564	0.28	0.29	6.4	3.5	0.364	1.80	94.2
8	0	183,300	375	634	0.38	0.50	13.8	3.3	0.315	1.69	185.9
	45	202,100	363	634	0.42	0.51	9.1	3.4	0.267	1.75	236.9
	90	173,500	296	582	0.39	0.46	7.3	3.2	0.349	1.97	228.6

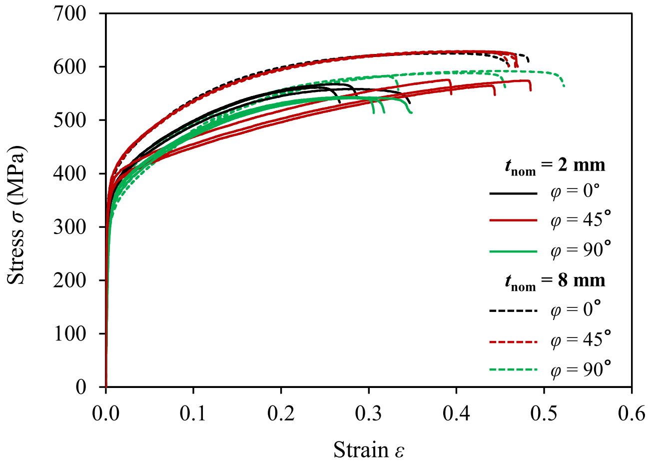

(a) Full range

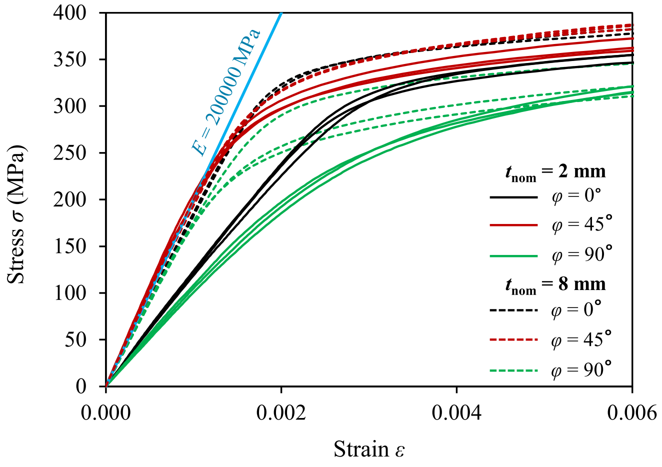

(b) Initial range

Fig. 14. Stress–strain curves from as-built coupons.

properties of the as-built coupons were calculated based on the average cross-sectional area determined via laser scanning and are referred to as ’effective’ properties; the effective mechanical properties are denoted with the subscript ‘eff’.

The as-built coupons exhibited good ductility, similar to that of the machined coupons, satisfying the Eurocode 3 ductility requirements of $\sigma_u/\sigma_{0.2} \geq 1.10$, $\varepsilon_f \geq 15\%$ and $\varepsilon_u/\varepsilon_y \geq 15$ [52,53]. Regarding the material anisotropy, the results of the tensile tests on the as-built coupons exhibited trends similar to those observed in the underlying material properties of the machined coupons, with the Young’s moduli of the coupons tested in the 0° and 90° directions being about 45% lower for the thinner specimens and 10% lower for the thicker specimens than both the 45° oriented coupons and the typical Young’s modulus value of 200000 MPa for conventional stainless steel.

6. Influence of as-built geometry and wall thickness

The influence of the undulating as-built surface on the mechanical properties of the LMD specimens was quantified by comparing the results of the as-built and machined coupon tests; the comparisons are summarised in Table 9.

The as-built geometry was found to have minimal influence on the mechanical properties, with all key material characteristics being almost the same between the machined and as-built coupons. This suggests that the undulating profile of the LMD surface is sufficiently smooth, as also evidenced by the low geometric variability, expressed as A_{sd}/A – see Table 4, to have an almost negligible impact on the static mechanical properties. A greater influence would nonetheless be expected under cyclic/fatigue conditions [54,55].

The influence of the wall thickness on the mechanical properties was found to be significant, with the thinner material exhibiting great anisotropy and generally reduced mechanical properties. Overall, most of the key mechanical properties exhibited by the thinner coupons for both surface finishes (i.e. machined and as-built) were lower compared to their thicker counterparts. As can be seen in Table 10 and Fig. 15, the most significant discrepancies were observed in the values of the Young’s modulus E, with the values for the 2 mm specimens being between about 30% and 40% lower than the 8 mm specimens in the 0° and 90° directions, but about 5% higher in the 45° direction. Smaller, but still notable differences were found in the strength values (up to 8% for $\sigma_{0.2}$ and 10% for σ_u), while the ductility measures followed similar trends to those observed for the Young’s moduli. The observed trends in mechanical properties are discussed and explained in the context of the findings from the microstructural analysis in the following section.

7. Correlation between microstructure and mechanical properties

The anisotropic mechanical response of AM stainless steels has been reported in several previous studies [36,40,56] and relates to the crystallographic texture, grain morphology and other features such as defects stemming from the fabrication process [57,58]. In this section, the correlation between key mechanical properties, such as the Young’s modulus, strength and ductility, and the observed microstructure of the examined LMD stainless steel are analysed and discussed.

7.1. Variation in Young’s modulus

The Young’s modulus of a single crystal in a given direction is dependent on the arrangement and bonding of the atoms. Calculation of the monocrystal elastic moduli of the examined austenitic stainless steel samples was undertaken using a set of formulae established by Armstrong *et al.* [59], used in conjunction with the monocrystal elastic stiffness constants determined experimentally by Ledbetter [60]. The calculated elastic moduli were 105.6 GPa in the <100> directions, 201.6 MPa in the <110> directions and 289.3 GPa in the <111>

Table 7
Effective mechanical properties of as-built coupons.

Coupon ID	E_{eff} (MPa)	$\sigma_{0.2,\mathrm{eff}}$ (MPa)	$\sigma_{\mathrm{u,eff}}$ (MPa)	$\varepsilon_{\mathrm{u,eff}}$	$\varepsilon_{\mathrm{f,eff}}$	n_{eff}	m_{eff}	ν_{eff}	$\sigma_{\mathrm{u,eff}}/\sigma_{0.2,\mathrm{eff}}$	$\varepsilon_{\mathrm{u,eff}}/\varepsilon_{\mathrm{y,eff}}$
AB-2-0-1	122,100	336	558	0.28	0.40	13.2	2.9	0.410	1.66	101.8
AB-2-0-2	124,500	344	567	0.26	0.35	12.9	2.7	0.398	1.65	94.1
AB-2-0-3	120,700	345	561	0.24	0.29	10.0	2.6	0.408	1.63	84.0
AB-2-45-1	204,100	337	565	0.44	0.47	10.1	2.3	−0.043	1.68	266.5
AB-2-45-2	216,900	347	576	0.39	0.43	8.9	2.4	−0.040	1.66	243.8
AB-2-45-3	217,000	337	574	0.48	0.52	7.9	2.5	−0.035	1.70	309.1
AB-2-90-1	107,600	303	543	0.28	0.36	5.4	3.3	0.368	1.79	99.4
AB-2-90-2	102,700	298	541	0.28	0.37	5.4	3.3	0.353	1.82	96.5
AB-2-90-3	112,700	295	542	0.30	0.31	5.5	3.2	0.346	1.84	114.6
AB-8-0-1	185,900	364	625	0.39	0.49	16.5	3.4	0.326	1.72	199.2
AB-8-0-2	181,800	365	627	0.40	0.52	16.0	3.4	0.335	1.72	199.2
AB-8-45-1	199,300	363	628	0.41	0.53	11.4	3.3	0.316	1.73	225.1
AB-8-45-2	195,200	364	629	0.41	0.51	11.7	3.3	0.242	1.73	219.9
AB-8-45-3	203,500	363	629	0.42	0.51	10.4	3.4	0.257	1.73	235.5
AB-8-90-1	180,600	329	582	0.32	0.36	11.7	2.8	0.328	1.77	175.7
AB-8-90-2	185,000	286	592	0.44	0.55	8.1	3.3	0.362	2.07	284.6
AB-8-90-3	179,700	297	588	0.41	0.49	8.3	3.2	0.357	1.98	248.1

Table 8
Average effective mechanical properties of as-built coupons.

t_{nom} (mm)	φ (°)	E_{eff} (MPa)	$\sigma_{0.2,\mathrm{eff}}$ (MPa)	$\sigma_{\mathrm{u,eff}}$ (MPa)	$\varepsilon_{\mathrm{u,eff}}$	$\varepsilon_{\mathrm{f,eff}}$	n_{eff}	m_{eff}	ν_{eff}	$\sigma_{\mathrm{u,eff}}/\sigma_{0.2,\mathrm{eff}}$	$\varepsilon_{\mathrm{u,eff}}/\varepsilon_{\mathrm{y,eff}}$
2	0	122,500	341	562	0.26	0.35	12.0	2.7	0.405	1.65	93.3
	45	212,700	340	571	0.44	0.47	8.9	2.4	−0.039	1.68	273.1
	90	107,700	299	542	0.29	0.34	5.4	3.3	0.356	1.81	103.5
8	0	183,800	364	626	0.39	0.51	16.3	3.4	0.330	1.72	199.2
	45	199,400	363	629	0.41	0.52	11.2	3.3	0.272	1.73	226.8
	90	181,700	304	588	0.39	0.47	9.4	3.1	0.349	1.94	236.1

Table 9
Comparison of average mechanical properties between as-built and machined coupons.

t_{nom} (mm)	φ (°)	E_{eff}/E	$\sigma_{0.2,\mathrm{eff}}/\sigma_{0.2}$	$\sigma_{\mathrm{u,eff}}/\sigma_{\mathrm{u}}$	$\varepsilon_{\mathrm{u,eff}}/\varepsilon_{\mathrm{u}}$
2	0	1.03	0.99	0.97	1.04
	45	1.00	0.99	0.99	0.94
	90	1.01	0.95	0.96	1.04
8	0	1.00	0.97	0.99	1.03
	45	0.99	1.00	0.99	0.98
	90	1.05	1.03	1.01	1.00

Table 10
Influence on wall thickness on average mechanical properties.

Surface	φ (°)	$\frac{E_{2\mathrm{mm}}}{E_{8\mathrm{mm}}}$	$\frac{\sigma_{0.2,2\mathrm{mm}}}{\sigma_{0.2,8\mathrm{mm}}}$	$\frac{\sigma_{\mathrm{u},2\mathrm{mm}}}{\sigma_{\mathrm{u},8\mathrm{mm}}}$	$\frac{\varepsilon_{\mathrm{u},2\mathrm{mm}}}{\varepsilon_{\mathrm{u},8\mathrm{mm}}}$	$\frac{\varepsilon_{\mathrm{f},2\mathrm{mm}}}{\varepsilon_{\mathrm{f},8\mathrm{mm}}}$
Machined	0	0.65	0.92	0.92	0.66	0.70
	45	1.05	0.95	0.91	1.12	1.02
	90	0.61	1.06	0.97	0.72	0.63
As-built	0	0.67	0.94	0.90	0.67	0.69
	45	1.07	0.94	0.91	1.07	0.90
	90	0.59	0.98	0.92	0.74	0.72

directions. The results of the EBSD analysis revealed a predominance of a <100> texture in the 0° and 90° directions in the 2 mm coupons, explaining the lower measured Young's modulus values in these directions, and a predominance of a <110> texture in the 45° direction, explaining the higher corresponding measured Young's modulus values – see Tables 4 and 5. The 8 mm machined coupons also showed higher Young's moduli in the $\varphi = 45°$ directions compared to the $\varphi = 0°$ and $\varphi = 90°$ directions, though to a lesser extent, due to the weaker crystallographic texture resulting from the employed printing strategy. Note that various studies [61,62] have similarly reported the significant influence of printing strategy on the texture and resulting mechanical properties of AM steels, underscoring the importance of selecting appropriate scan strategies to achieve the desired material properties.

7.2. Variation in strength

The 0.2% proof strength and ultimate strength of the 8 mm material were generally higher (by up to about 10%) compared to the 2 mm material; this accords with the observed finer grain size in the 8 mm LMD stainless steel. A degree of anisotropy in the strength was also observed, with the $\varphi = 0°$ and $\varphi = 45°$ machined coupons exhibiting approximately 10% and 20% higher 0.2% proof strengths than the $\varphi = 90°$ machined coupons for the 2 mm and 8 mm material, respectively. Anisotropy in the strength of AM metallic materials has been widely studied and attributed to several factors, including crystallographic texture [58,63], elongated grains relative to the loading direction [64], inter-layer/track defects [65] and mechanisms such as twinning or dislocation slip [57,63]. The dominant mechanism governing deformation behaviour depends on the loading direction. The 2 mm LMD stainless steel samples exhibited a strong <100> texture along the SD (i.e. $\varphi = 0°$), BD (i.e. $\varphi = 90°$) and TD axes, and a <110> texture along $\varphi = 45°$, as well as a high proportion of elongated grains with large aspect ratios. The lower 0.2% proof strength observed in the 2 mm machined coupons when loaded in the BD can be explained by the crystallographic texture and the presence of elongated grains with their long axes aligned along the BD axis. This results in a larger effective grain size along the BD axis, potentially leading to reduced grain boundary strengthening as described by the Hall-Petch relationship [65,66]. In contrast, the 8 mm LMD stainless steel exhibited a weaker texture, with columnar grains oriented either along or at 45° to the BD axis. The anisotropy in the 0.2% proof and ultimate strengths of the 8 mm stainless steel is attributed to the alignment of elongated grains relative to the loading directions.

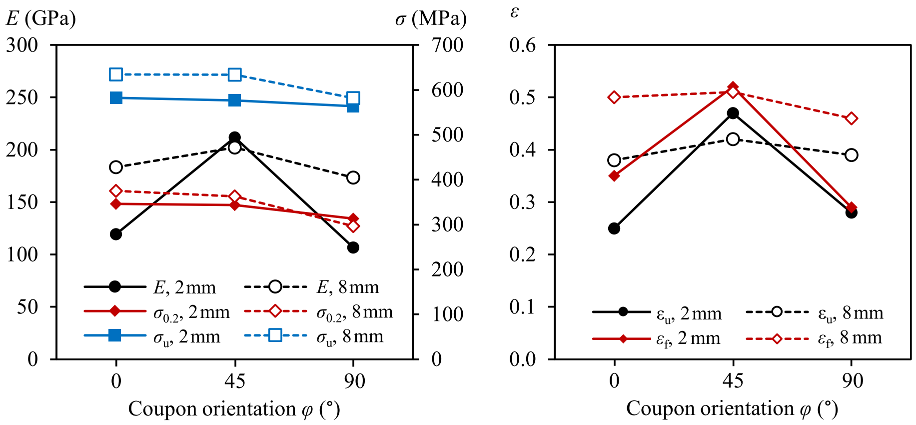

Fig. 15. Comparison of key mechanical properties between thinner and thicker machined material.

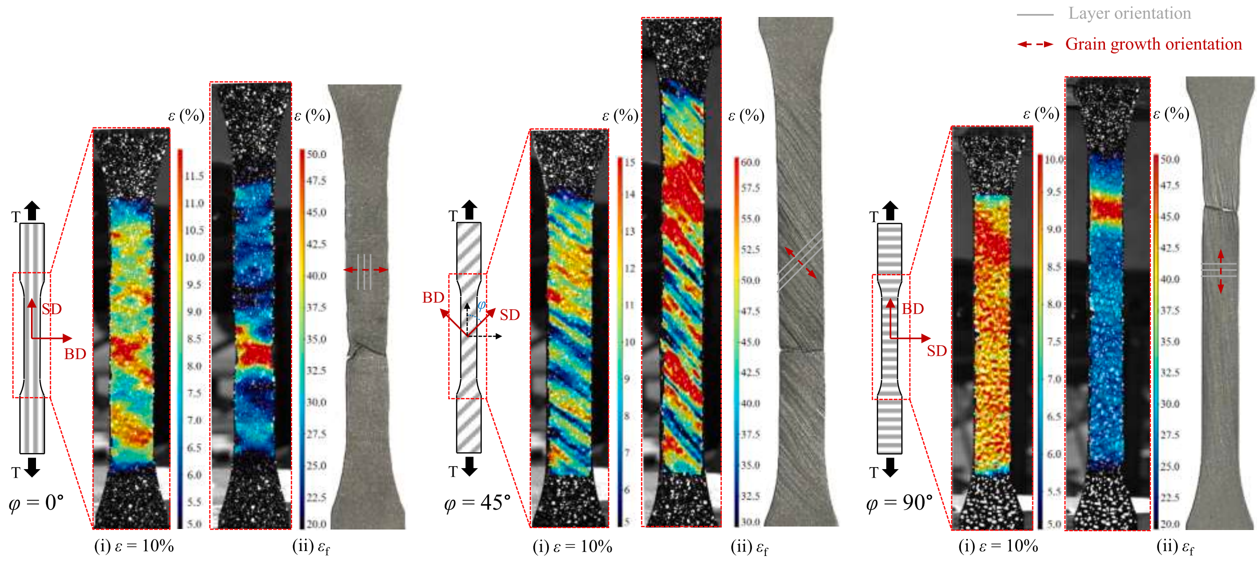

Fig. 16. Typical deformation profiles of 2 mm machined coupons with overlaid longitudinal strain fields at (i) 10% strain and (ii) fracture.

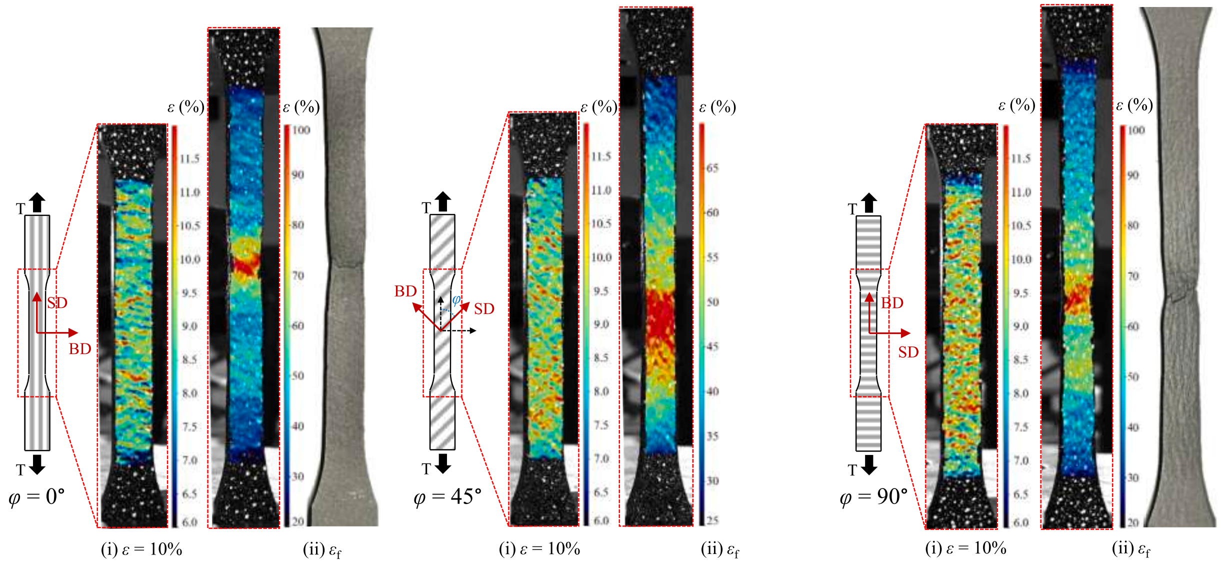

Fig. 17. Typical deformation profiles of 8 mm machined coupons with overlaid longitudinal strain fields at (i) 10% strain and (ii) fracture.

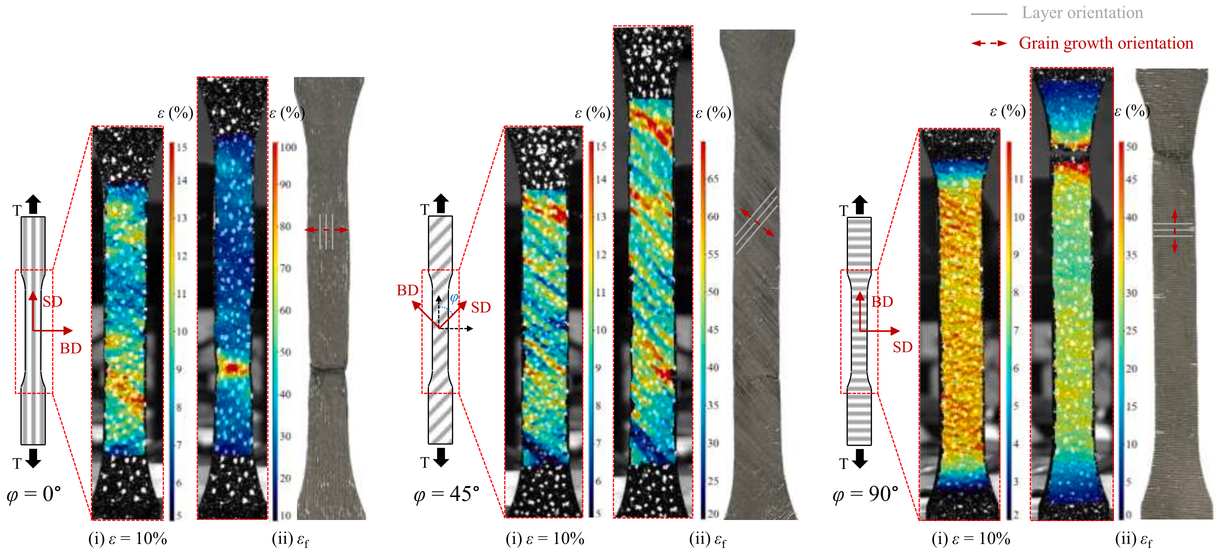

Fig. 18. Typical deformation profiles of 2 mm as-built coupons with overlaid longitudinal strain fields at (i) 10% strain and (ii) fracture.

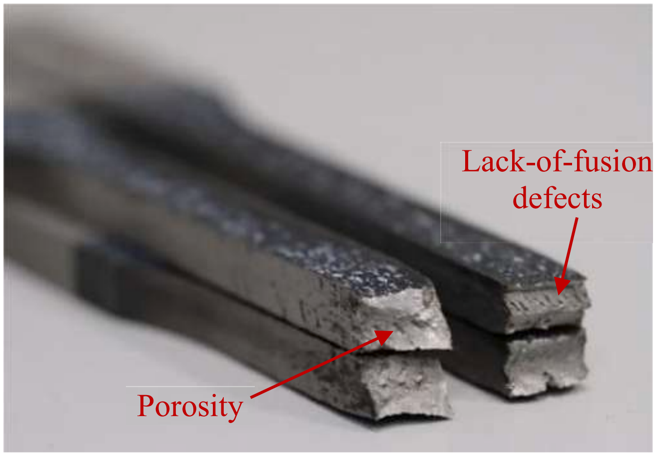

Fig. 19. Fracture surfaces of coupons M-8–90-1 and M-8–90-3.

7.3. *Variation in ductility*

Typical deformation profiles with overlaid longitudinal strain fields at (i) 10% strain and (ii) fracture are shown in Figs. 16 and 17 for the 2 mm and 8 mm machined coupons, respectively, and in Fig. 18 for the 2 mm as-built coupons. Multiple strain localisation bands parallel to the BD (i.e. in the grain growth direction) can be seen in the $\varphi = 0^\circ$ and $\varphi = 45^\circ$ 2 mm coupons, while the $\varphi = 90^\circ$ coupons exhibited a relatively uniform strain distribution before necking.

The fracture strains ε_f of the $\varphi = 0^\circ$ and $\varphi = 90^\circ$ 2 mm machined coupons were similar, while the $\varphi = 45^\circ$ coupons had higher fracture strains. Previous studies have reported such anisotropic ductility in WAAM and LMD stainless steels and linked it to the melt pool macrostructure [67] and interlayer lack-of-fusion defects [64]. The measured fracture strains of the 8 mm machined coupons showed no significant differences across various loading directions due to the employed printing strategy, with the exception of the M-8–90-1 and M-8–90-3 coupons, the fracture surfaces of which had visible signs of interlayer porosity and lack-of-fusion defects – see Fig. 19.

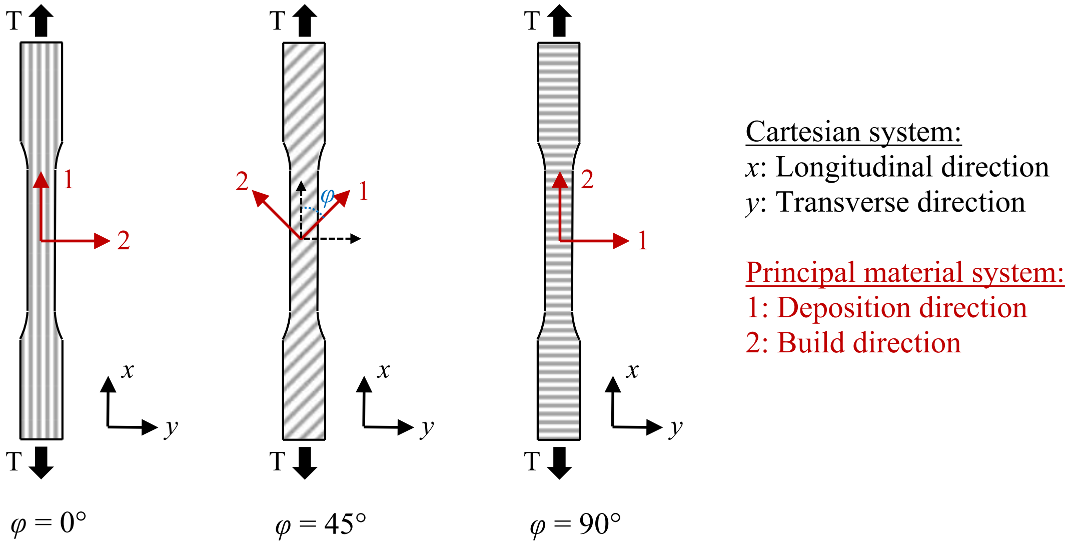

Fig. 20. Material orientation of examined coupons and adopted coordinate systems.

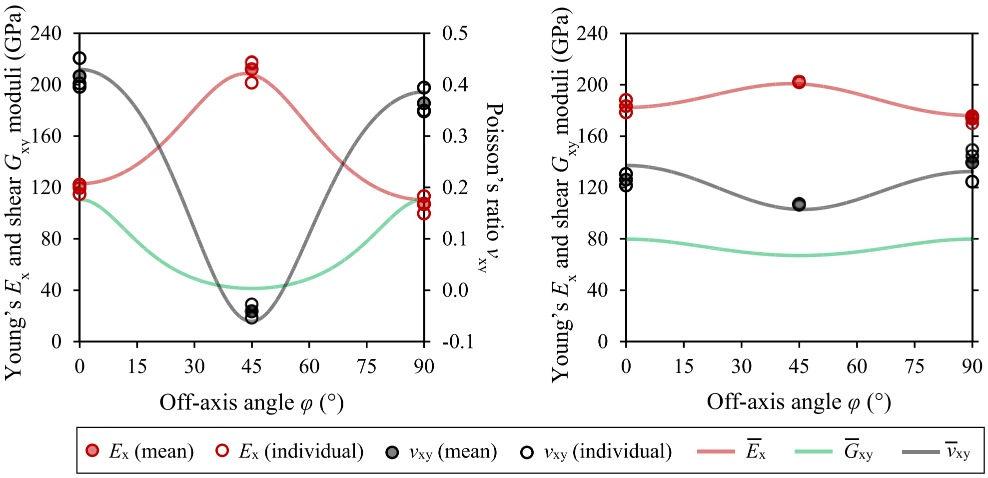

(a) t_{nom} = 2 mm   (b) t_{nom} = 8 mm

Fig. 21. Variation of elastic constants with φ in the machined coupons.

Table 11
Optimised values of elastic constants for machined coupons.

t_{nom} (mm)	φ (°)	$\overline{E}_x$ (GPa)	$\overline{E}_y$ (GPa)	$\overline{\nu}_{xy}$	$\overline{G}_{xy}$ (GPa)
2	0	122.9	110.4	0.430	110.7
	45	207.9	207.9	−0.061	41.3
	90	110.4	122.9	0.386	110.7
8	0	182.4	176.1	0.343	79.8
	45	200.7	200.7	0.257	67.0
	90	176.1	182.4	0.331	79.8

Table 12
Optimised values of elastic constants for as-built coupons.

t_{nom} (mm)	φ (°)	$\overline{E}_{x,eff}$ (GPa)	$\overline{E}_{y,eff}$ (GPa)	$\overline{\nu}_{xy,eff}$	$\overline{G}_{xy,eff}$ (GPa)
2	0	125.7	112.0	0.422	110.9
	45	208.4	208.4	−0.060	42.4
	90	112.0	125.7	0.376	110.9
8	0	182.8	182.2	0.338	78.4
	45	199.8	199.8	0.275	68.2
	90	182.2	182.8	0.337	78.4

8. Characterisation of mechanical response

In this section, the anisotropic behaviour of the LMD material in the elastic range is characterised using an orthotropic plane stress material model, based on the framework established by Hadjipantelis *et al.* for WAAM stainless steels [68]. Fig. 20 illustrates the adopted coordinate systems, where the principal material coordinate system is positioned at an angle φ relative to the Cartesian coordinate system of the coupons (*x*-*y*-*z*). In this context, the *x*, *y* and *z* axes correspond to the longitudinal (loading), transverse and out-of-plane directions, respectively, while the angle φ represents the orientation of the loading direction relative to the deposition direction.

Unlike fully anisotropic material models, which have 21 independent elastic constants, orthotropic models have only nine: three Young's moduli, three Poisson's ratios and three shear moduli. In addition, given the thin-walled nature of the LMD material examined herein, the assumption of plane stress conditions (in the 1–2 plane as per Fig. 20) is reasonable, which further reduces the number of independent constants to 4, namely two Young's moduli E_1 and E_2 in the 1 and 2-directions, respectively, one Poisson's ratio $\nu_{12} = -\varepsilon_2/\varepsilon_1$ equal to the ratio of the transverse to the longitudinal strains when stress is applied in the 1-direction, and one shear modulus G_{12} in the 1–2 plane. Thus, in line with Fig. 21, the following relationships are adopted: (i) $E_1 = E_{x,0°} = E_{y,90°}$, (ii) $E_2 = E_{x,90°} = E_{y,0°}$, (iii) $E_{x,45°} = E_{y,45°}$, (iv) $\nu_{12} = \nu_{xy,0°} = \nu_{yx,90°}$, (v) $\nu_{21} = \nu_{xy,90°} = \nu_{yx,0°}$ and (vi) $\nu_{xy,45°} = \nu_{yx,45°}$. The optimisation process described in [68] was also employed herein to minimise the difference between the experimentally measured properties (i.e. the average Young's moduli $E_{x,0°}$, $E_{x,45°}$ and $E_{x,90°}$ and the average Poisson's ratios $\nu_{xy,0°}$, $\nu_{xy,45°}$ and $\nu_{xy,90°}$) and the corresponding values predicted by the orthotropic material model. These optimised values, denoted with macrons ($\bar{\ }$), are reported in Tables 11 and 12 for the machined and as-built coupons respectively.

In Figs. 21 and 22, the theoretical variation of the elastic properties calculated using the optimised values listed in Tables 10 and 11 are plotted against the off-axis angle φ for the machined and as-built coupons, respectively. The individual and average values of the measured elastic properties determined from the tensile tests are also illustrated, with hollow and solid markers respectively. It is evident that the variation in the elastic constants of the LMD material with respect to the off-axis angle φ are almost symmetrical about the angle $\varphi = 45°$, both for the machined and as-built specimens. Note that, the occurrence of effective Poisson's ratios approximately equal to zero in several $\varphi = 45°$ coupons is linked to the preferred crystallographic texture, as discussed in Section 5.2.

Regarding the inelastic material response, this was described using the Hill yield surface [69] for plane stress conditions, which is an extension of the von Mises criterion for isotropic materials [70]. The Hill model requires the yield stress in three different directions relative to the chosen reference direction, which in this study is set at $\varphi = 0°$ [68]. Following the process described in detail in [68] and using the average 0.2% proof stresses listed in Tables 5 and 7 for the machined and as-built material respectively, the values of the anisotropic yield stress ratios R_{11}, R_{22} and R_{12} were obtained and are reported in Table 13. Note that for the plane stress conditions assumed herein, R_{33} is set equal to unity.

The yield surfaces for all coupons, determined based on the Hill criterion using the average 0.2% proof stresses, are illustrated in Fig. 23. The stresses along the axes 1 and 2 (as per Fig. 20) are denoted by σ_1 and σ_2 respectively, while σ^0 denotes the reference yield strength. For comparison, the von Mises yield surfaces, corresponding to an isotropic material response, are also shown. As shown in Fig. 23, the asymmetry of the Hill yield surface intensifies with increasing wall thickness, indicating a more pronounced anisotropic response. It is further

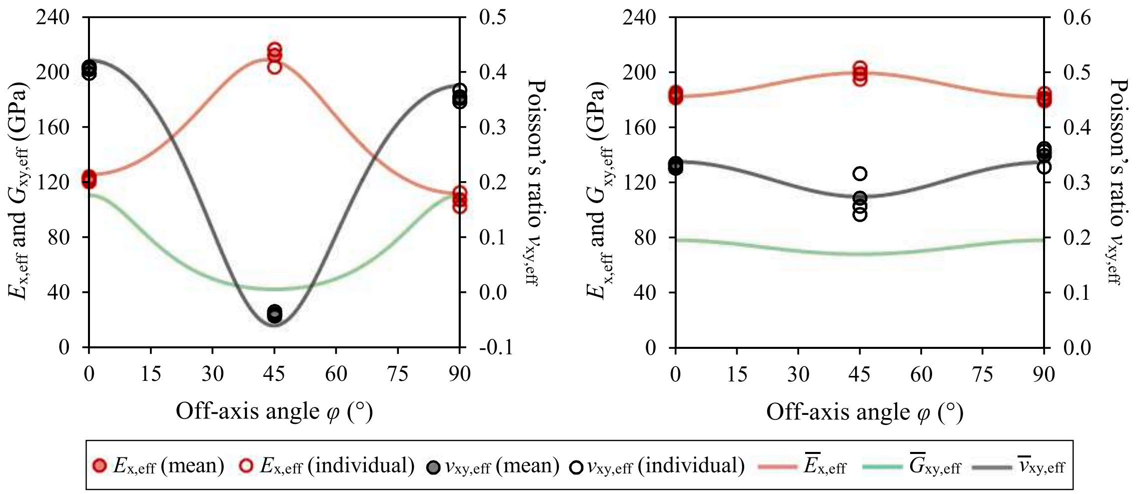

(a) $t_{nom} = 2$ mm

(b) $t_{nom} = 8$ mm

Fig. 22. Variation of effective elastic constants with φ in the as-built coupons.

Table 13
Average R-values with $\varphi = 0°$ taken as the reference direction.

Surface finish	t_{nom} (mm)	R_{11}	R_{22}	R_{33}	R_{12}
Machined	2	1	0.905	1	0.989
	8	1	0.790	1	0.956
As-built	2	1	0.875	1	0.995
	8	1	0.834	1	0.996

illustrated that increasing geometric variability is also influential, albeit to a lesser degree, as can be seen by comparing the machined and as-built samples of same thickness. The effects of the geometric variability on the yield surface of the examined LMD austenitic stainless steel are more clearly demonstrated in Fig. 24, where the Hill surfaces for all coupon types are plotted together. It can be observed that the machined coupons demonstrate a slightly higher yielding resistance under most stress combinations.

9. Conclusions

A thorough experimental investigation conducted to obtain insight into the mechanical properties and microstructure of LMD plates fabricated from ER 308LSi austenitic stainless steel wire has been presented. Tensile tests were performed on LMD coupons with different surface conditions, thicknesses and extraction orientations. Both as-built and machined coupons were tested to assess the impact of the surface geometric undulations on the stress–strain response, while material anisotropy was explored by testing specimens at 0°, 45° and 90° relative to the print layer orientation.

Advanced non-contact measurement techniques, featuring laser scanning and digital image correlation, were employed to accurately capture the geometric properties and deformation fields of the specimens. Microstructural characterisation using scanning electron microscopy and electron backscatter diffraction (EBSD) was also carried out to obtain insight into the microstructure of the examined material.

The test results showed that the LMD coupons exhibited good ductility, satisfying the Eurocode 3 ductility requirements. The geometric irregularity arising as a result of the LMD process was found to be minimal, with the mechanical properties of the machined and as-built specimens being nearly identical.

The tests revealed substantial material anisotropy, with the stress–-strain characteristics being strongly influenced by the loading direction. EBSD analysis revealed a strong crystallographic texture, particularly in the thinner specimens, dominated by elongated columnar grains, which explained the observed anisotropic mechanical properties. Finally, a modelling approach previously developed for WAAM stainless steel was successfully adapted to characterise the anisotropic behaviour of LMD stainless steel in both the elastic and inelastic regimes.

Overall, it has been shown that LMD stainless steel, when manufactured using suitable printing parameters, exhibits excellent mechanical properties, highlighting the feasibility and potential of using LMD stainless steel for load-bearing applications. However, the possible mechanical anisotropy resulting from the layer-by-layer deposition process and discrepancies between nominal and measured strengths require further investigation and should be carefully considered in the

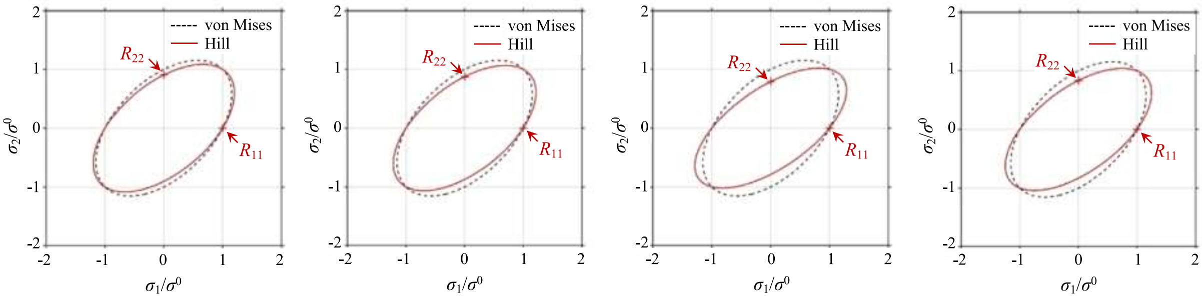

(a) 2 mm, machined

(b) 2 mm, as-built

(c) 8 mm, machined

(d) 8 mm, as-built

Fig. 23. Normalised yield surfaces for all coupon types using the von Mises and Hill yield criteria.

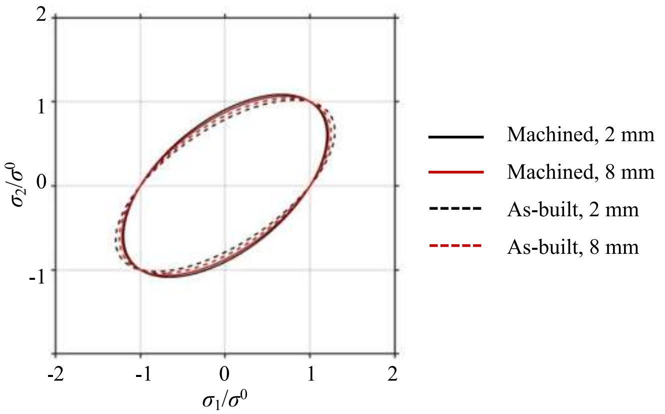

Fig. 24. Comparison of the yield surfaces of all coupons based on the Hill yield criterion.

design process.

CRediT authorship contribution statement

P. Kyvelou: Writing – review & editing, Writing – original draft, Visualization, Supervision, Project administration, Methodology, Investigation, Funding acquisition, Formal analysis, Conceptualization. **W. Hong:** Visualization, Software, Methodology, Investigation, Formal analysis, Data curation. **R. Zhang:** Writing – review & editing, Writing – original draft, Visualization, Software, Methodology, Investigation, Formal analysis, Data curation. **L. Gardner:** Writing – review & editing, Supervision, Resources, Project administration, Methodology, Funding acquisition, Conceptualization.

Declaration of competing interest

The authors declare that they have no known competing financial interests or personal relationships that could have appeared to influence the work reported in this paper.

Acknowledgements

The authors would like to thank Meltio for providing the test specimens and Paul Crudge and Freddy Olivo at Imperial College London for their assistance in the experimental programme.

Data availability

Data will be made available on request.

References

[1] L. Gardner, (2023) Metal additive manufacturing in structural engineering – review, advances, opportunities and outlook, Structures 47 (2023) 2178–2193.
[2] I.H. Shah, N. Hadjipantelis, L. Walter, R.J. Myers, L. Gardner, Environmental life cycle assessment of wire arc additively manufactured structural components, J. Clean. Prod. 389 (2023) 136071.
[3] Meng X, Gardner L. Hybrid construction featuring wire arc additive manufacturing: review, concepts, challenges and opportunities. Engineering Structures. [Submitted].
[4] A. Kanyilmaz, A.G. Demir, M. Chierici, F. Berto, L. Gardner, S.Y. Kandukuri, P. Kassabian, T. Kinoshita, A. Laurenti, I. Paoletti, A. du Plessis, N. Razavi, Role of metal 3D printing to increase quality and resource-efficiency in the construction sector, Addit. Manuf.. 50 (2022) 102541.
[5] R. Rumman, D.A. Lewis, J.Y. Hascoet, J.S. Quinton, Laser metal deposition and wire arc additive manufacturing of materials: An overview, Arch. Metall. Mater.. 64 (2) (2019) 467–473.
[6] E. Ghafoori, H. Dahaghin, C. Diao, N. Pichler, L. Li, M. Mohri, J. Ding, S. Ganguly, S. Williams, Fatigue strengthening of damaged steel members using wire arc additive manufacturing, Eng. Struct.. 284 (2023) 115911.
[7] X. Guo, P. Kyvelou, J. Ye, L.H. Teh, L. Gardner, Experimental study of DED-arc additively manufactured steel double-lap shear bolted connections, Eng. Struct.. 281 (2023) 115736.
[8] B. Weber, X. Meng, R. Zhang, M. Nitawaki, T. Sagawa, L. Gardner, Tensile behaviour of WAAM high strength steel material and members, Mater. Des.. 237 (2024) 112517.
[9] J. Ye, P. Kyvelou, F. Gilardi, H. Lu, M. Gilbert, L. Gardner, An end-to-end framework for the additive manufacture of optimized tubular structures, IEEE Access. 9 (2021) 165476–165489.
[10] P. Kyvelou, A. Spinasa, L. Gardner, Testing and Analysis of Optimized Wire Arc Additively Manufactured Steel Trusses, J. Struct. Eng.. 150 (3) (2024) 04024008.
[11] L. Gardner, J. Li, X. Meng, C. Huang, P. Kyvelou, I-section steel columns strengthened by wire arc additive manufacturing - concept and experiments, Eng. Struct.. 306 (2024) 117763.
[12] V. Laghi, M. Palermo, M. Bruggi, G. Gasparini, T. Trombetti, Blended structural optimization for wire-and-arc additively manufactured beams, Prog. Addit. Manuf.. 8 (2023) 381–392.
[13] S.I. Evans, F. Xu, J. Wang, Material properties and local stability of WAAM stainless steel equal angle sections, Eng. Struct.. 287 (2023) 116160.
[14] Chen MT, Y, Zuo W, Yun X, Zhao O, Liu SW, Xu F. Experimental investigation on the tensile behavior of wire arc additively manufactured duplex stainless steel plates. Engineering Structures. 2024; 321: 118764.
[15] M.T. Chen, Z. Gong, T. Zhang, W. Zuo, Y. Zhao, O. Zhao, G. Zhang, Z. Wang, Mechanical behavior of austenitic stainless steels produced by wire arc additive manufacturing, Thin-Walled Struct.. 196 (2024) 111455.
[16] M. Kucukler, Z. Xing, L. Gardner, Behaviour and design of stainless steel I-section columns in fire, J. Constr. Steel Res.. 165 (2020) 105890.
[17] O. Zhao, B. Rossi, L. Gardner, B. Young, Experimental and numerical studies of ferritic stainless steel cross-sections under combined compression and bending, J. Struct. Eng. ASCE. 142 (2) (2016) 04015110.
[18] M. Bock, L. Gardner, E. Real, Material and local buckling response of ferritic stainless steel sections, Thin-Walled Struct.. 89 (2015) 131–141.
[19] G. Gong, J. Ye, Y. Chi, Z. Zhao, Z. Wang, G. Xia, X. Du, H. Tian, H. Yu, C. Chen, Research status of laser additive manufacturing for metal: a review, J. Mater. Res. Technol.. 15 (2021) 855–884.
[20] T. DebRoy, H.L. Wei, J.S. Zuback, T. Mukherjee, J.W. Elmer, J.O. Milewski, A. M. Beese, A. Wilson-Heid, A. De, W. Zhang, Additive manufacturing of metallic components - Process, structure and properties, Prog. Mater Sci. 92 (2018) 112–224.
[21] I. Gibson, D. Rosen, B. Stucker, Additive Manufacturing Technologies: 3D Printing, Rapid Prototyping, and Direct Digital Manufacturing, Springer, 2014.
[22] N. Ghanadi, S. Pasebani, A Review on Wire-Laser Directed Energy Deposition: Parameter Control, Process Stability, and Future Research Paths, Manufacturing and Materials Processing. 8 (2) (2024) 84.
[23] S. Vock, A. Kozak, Additive manufacturing for the aerospace industry, Mater. Today. 21 (1) (2018) 22–23.
[24] A.H. Alami, A. Ghani Olabi, A. Alashkar, S. Alasad, H. Aljaghoub, H. Rezk, M. A. Abdelkareem, Additive manufacturing in the aerospace and automotive industries: Recent trends and role in achieving sustainable development goals, Ain Shams Eng. J.. 14 (11) (2023) 102516.
[25] M. Ahmad, M. Javaid, A. Haleem, Enhancing biocompatible metal alloy fabrication for bio implants through laser-based additive manufacturing (LBAM), Biomedical Analysis. 1 (1) (2024) 73–85.
[26] S. Attarilar, M. Ebrahimi, F. Djavanroodi, Y. Fu, L. Wang, J. Yang, 3D Printing Technologies in Metallic Implants: A Thematic Review on the Techniques and Procedures, Internation Journal of Bioprinting. 7 (1) (2020) 306.
[27] A. Menghini, S. Maffia, A.G. Demir, A. Kanyilmaz, F. Berto, C.A. Castiglioni, B. Previtali, Performance of laser metal deposition on hot-rolled stainless steel for hybrid steel structures, Constr. Build. Mater.. 443 (2024) 137744.
[28] J. Pasco, Z. Lei, C. Aranas Jr., Additive Manufacturing in Off-Site Construction: Review and Future Directions, Buildings. 12 (2022) 53.
[29] S.I. Evans, J. Wang, J. Qin, Y. He, P. Shepherd, J. Ding, A review of WAAM for steel construction-Manufacturing, material and geometric properties, design, and future directions, Structures. 44 (2022) 1506–1522.
[30] V. Laghi, L. Tonelli, M. Palermo, M. Bruggi, R. Sola, L. Ceschini, T. Trombetti, Experimentally-validated orthotropic elastic model for Wire-and-Arc Additively Manufactured stainless steel, Addit. Manuf.. 42 (2021) 101999.
[31] V. Laghi, M. Palermo, G. Gasparini, V.A. Girelli, T. Trombetti, On the influence of the geometrical irregularities in the mechanical response of wire-and-arc additively manufactured planar elements, J. Constr. Steel Res.. 178 (2021) 106490.
[32] L.P. Belotti, J.A.W. van Dommelen, M.G. Geers, W. Ya, J.P. Hoefnagels, Influence of the printing strategy on the microstructure and mechanical properties of thick-walled wire arc additive manufactured stainless steels, J. Mater. Process. Technol.. 324 (2024) 118275.
[33] D.D. Gu, W. Meiners, K. Wissenbach, R. Poprawe, Laser additive manufacturing of metallic components: materials, processes and mechanisms, Int. Mater. Rev.. 57 (3) (2012) 133–164.
[34] Meltio. Wire-Laser Metal 3D printing. https://meltio3d.com/ [Accessed 2nd September 2024].
[35] E.N. Iso, 6892–1:2019., Metallic materials - Tensile testing - Part 1: Method of test at room temperature, European committee for standardization, Brussels, 2019.
[36] P. Kyvelou, H. Slack, D. Daskalaki-Mountanou, M.A. Wadee, T.B. Britton, C. Buchanan, L. Gardner, Mechanical and microstructural testing of wire and arc additively manufactured sheet material, Mater. Des.. 192 (2020) 108675.

[37] C. Huang, P. Kyvelou, R. Zhang, T.B. Britton, L. Gardner, Mechanical testing and microstructural analysis of wire arc additively manufactured steels, Mater. Des.. 216 (2022) 110544.

[38] Oqton, Inc, Geomagic Wrap 2017, https://www.oqton.com/geomagic-wrap, Version 2017.0.2:64.

[39] Robert McNeel & Associates, Rhino 6, https://www.rhino3d.com/, Version 6.

[40] R. Zhang, C. Buchanan, V.P. Matilainen, D. Daskalaki-Mountanou, T.B. Britton, H. Piili, A. Salminen, L. Gardner, Mechanical properties and microstructure of additively manufactured stainless steel with laser welded joints, Mater. Des.. 208 (2021) 109921.

[41] ASTM E3-11:2017. Standard Guide for Preparation of Metallographic Specimens., West Conshohocken, PA: American Society for Testing and Materials; 2017.

[42] Bruker Corporation, ESPRIT, https://www.bruker.com/en/products-and-solutions/elemental-analyzers/eds-wds-ebsd-SEM-Micro-XRF/software-esprit-family.html,Version 2.3.

[43] F. Bachmann, R. Hielscher, H. Schaeben, Texture analysis with MTEX–free and open source software toolbox, Solid State Phenom.. 160 (2010) 63–68.

[44] ASTM E2627-23. Standard practice for determining average grain size using electron backscatter diffraction (EBSD) in fully polycrystalline materials. Technical Report, West Conshohocken, PA: ASTM International; 2013.

[45] E.N. Iso, 6507–1:2018., Metallic materials - Vickers hardness test - Part 1: Test method, European committee for standardization, Brussels, 2018.

[46] Ramberg W, Osgood WR. Description of stress-strain curves by three parameters. Technical Note No. 902, National Advisory Committee for Aeronautics. Washington, D.C., USA; 1943.

[47] K.J.R. Rasmussen, Full-range stress–strain curves for stainless steel alloys, J. Constr. Steel Res.. 59 (1) (2003) 47–61.

[48] LaVision GmbH, DaVis 10, https://www.lavision.de/en/products/davis-software/, Version 10.2.1.

[49] O. Zhao, L. Gardner, B. Young, Behaviour and design of stainless steel SHS and RHS beam-columns, Thin-Walled Struct.. 106 (2016) 330–345.

[50] I. Arrayago, E. Real, L. Gardner, Description of stress-strain curves for stainless steel alloys, Mater. Des.. 87 (2015) 540–552.

[51] X. Yun, Z. Wang, L. Gardner, Full-range stress-strain curves for aluminum alloys, J. Struct. Eng. ASCE. 147 (6) (2021) 04021060.

[52] B.S. En, 1993-1-4:2006., Eurocode 3. Design of steel structures - General rules. Supplementary rules for stainless steels, European committee for standardization, Brussels, 2006.

[53] EN 1993-1-1:2020. Eurocode 3 - Design of steel structures - Part 1-1: General rules and rules for buildings. Brussels: European committee for standardization; 2020.

[54] L. Zong, W. Fang, C. Huang, Z. Wang, L. Gardner, Low cycle fatigue behaviour of wire arc additively manufactured ER70S-6 steel, Int. J. Fatigue. 176 (2023) 107910.

[55] C. Huang, L. Li, N. Pichler, E. Ghafoori, L. Susmel, L. Gardner, Fatigue testing and analysis of steel plates manufactured by wire-arc directed energy deposition, Addit. Manuf.. 73 (2023) 103696.

[56] R. Zhang, M. Amraei, H. Piili, L. Gardner, Microstructure, mechanical properties and cross-sectional behaviour of additively manufactured stainless steel cylindrical shells, Thin-Walled Struct.. 208 (2024) 112750.

[57] X. Wang, J.A. Muñiz-Lerma, M.A. Shandiz, O. Sanchez-Mata, M. Brochu, Crystallographic-orientation-dependent tensile behaviours of stainless steel 316L fabricated by laser powder bed fusion, Mater. Sci. Eng. A. 766 (2019) 138395.

[58] Weaver JS, Rosenthal I. Understanding anisotropic tensile properties of laser powder bed fusion additive metals: a detailed review of select examples. US Department of Commerce, National Institute of Standards and Technology; 2021.

[59] D.E. Armstrong, A.J. Wilkinson, S.G. Roberts, Measuring anisotropy in Young's modulus of copper using microcantilever testing, J. Mater. Res.. 24 (2009) 3268–3276.

[60] H.M. Ledbetter, Predicted monocrystal elastic constants of 304-type stainless steel, Physica B+c 128 (1) (1985) 1–4.

[61] D. Leonetti, M. de Munnik, L. Kassing, D. Khan, J.F. Moulin, B. Snijder, Rotating bending fatigue behaviour and quasi-static tensile properties of Wire Arc Additively Manufactured 308L stainless steel, Ce/papers. 6 (3–4) (2023) 732–738.

[62] O. Zinovieva, V. Romanova, R. Balokhonov, Effects of scanning pattern on the grain structure and elastic properties of additively manufactured 316L austenitic stainless steel, Mater. Sci. Eng. A. 832 (2022) 142447.

[63] A. Charmi, R. Falkenberg, L. Ávila, G. Mohr, K. Sommer, A. Ulbricht, A. Evans, Mechanical anisotropy of additively manufactured stainless steel 316L: An experimental and numerical study, Mater. Sci. Eng. A. 799 (2021) 140154.

[64] M. Mukherjee, Effect of build geometry and orientation on microstructure and properties of additively manufactured 316L stainless steel by laser metal deposition, Materialia. 7 (2019) 100359.

[65] E.O. Hall, The deformation and ageing of mild steel: III discussion of results, Proc. Phys. Soc. – Section B. 64 (9) (1951) 747.

[66] N.J. Petch, The cleavage strength of polycrystals, The Journal of the Iron and Steel Institute. 174 (1953) 25–28.

[67] L.P. Belotti, T.F.W. Van Nuland, M.G.D. Geers, J.P.M. Hoefnagels, J.A.W. Van Dommelen, On the anisotropy of thick-walled wire arc additively manufactured stainless steel parts, Mater. Sci. Eng. A 863 (2023) 144538.

[68] N. Hadjipantelis, B. Weber, C. Buchanan, L. Gardner, Description of anisotropic material response of wire and arc additively manufactured thin-walled stainless steel elements, Thin-Walled Struct.. 171 (2022) 108634.

[69] Hill R. A theory of the yielding and plastic flow of anisotropic metals. Proceedings of the Royal Society A: Mathematical, Physical and Engineering Sciences. 1948; 193: 281-297.

[70] R. von Mises, Mechanik der plastischen Formänderung von Kristallen, J. Appl. Math. Mech.. 8 (1928) 161–185.